WIND TUNNEL TEST OF A ROTORCRAFT WITH LIFT COMPOUNDING

André Bauknecht, a.bauknecht@tu-braunschweig.de, Institute for Fluid Mechanics, Technical University Braunschweig, Germany and Alfred Gessow Rotorcraft Center, University of Maryland, USA
Xing Wang, wxing99@umd.edu, Alfred Gessow Rotorcraft Center, University of Maryland, USA
Inderjit Chopra, chopra@umd.edu, Alfred Gessow Rotorcraft Center, University of Maryland, USA

Abstract
A recent doctrine in rotorcraft development is the pursuit of higher flight speeds. Limiting factors are compressibility effects on the advancing blade side and decreasing lift potential on the retreating blade side. It may therefore be beneficial to employ a hingeless rotor to generate additional lift on the advancing blade side and compensate the resulting rolling moment with a fixed-wing on the retreating blade side. This concept is a form of “lift-compounding” that has not been studied in detail yet. The present paper presents results of a wind tunnel test with a slowed, hingeless rotor and single fixed-wing (0.7*R* span, 0.24*R* below rotor plane) on the retreating blade side. Based on rotor test stand data and flow field measurements, the impact of operational and rotor parameters on performance and flow field of the system is examined, mutual interaction effects between rotor and fixed-wing are analyzed, and dominant flow structures are characterized in the reverse flow region on the retreating blade side. Flow field analysis reveals a dynamic stall vortex that freely convects through the reverse flow region and rivals the blade tip vortices in strength. Contrary to previous beliefs, this vortex originates from upstream of the reverse flow region and only its detachment from the rotor blade is related to entering this region. Advance ratio and shaft tilt angle are found to have significant and non-linear impact on the dynamic stall vortex and its interactions with rotor blades and other vortices. The rotor downwash reduces fixed-wing lift by up to 23% and increases its vibratory loads, while the fixed-wing is found to influence the effective angle of attack of the retreating rotor blade by up to 2 deg. The combination of finite rolling moment trim and aft shaft tilt increases the rotor lift coefficient by up to about 79% at 6 deg rotor collective and the corresponding peak lift-to-drag ratio of the compound rotorcraft is improved by up to 60% at $\mu = 0.5$. Results are compared with predictions from a comprehensive rotor analysis code that is expanded to cover the main effects of added fixed-wing and is able to reproduce general performance trends of the rotorcraft. The present study highlights that adding a single fixed-wing to a high-speed hingeless rotor could significantly improve its performance.

NOMENCLATURE

AR	Wing aspect ratio
A_R	Rotor disk area, m
b_W	Wing span, m
c_R	Rotor blade chord length, m
c_W	Wing chord length at 30%R span, m
C_H	Rotor in-plane load, N
C_L	Lift coefficient, $C_L = L/\rho_\infty \pi R^2 (\Omega R)^2$
C_Q	Torque coefficient, $C_Q = Q/\rho_\infty \pi R^2 (\Omega R)^2$
D_R	Rotor drag, N
D_e	Equivalent rotor drag, $D_e = Q\Omega/V_\infty + D_R$, N
$EI_{x,y}$	Lag/flap bending stiffness, N-mm^2
GJ	Torsional stiffness, N-mm^2
LS	Lift share ratio, $LS = L_W/(L_R+L_W)$
L_R	Vertical rotor lift component, N
L_W	Fixed-wing lift, N
M_x	Hub rolling moment, Nm
n	Vatistas vortex model parameter
Q	Rotor shaft torque, Nm
R	Rotor radius, m
r_c	Vortex core radius, m
T	Rotor thrust, N
u,v,w	Flow velocities in x,y,z direction, m/s
V_{swirl}	Vortex tangential velocity, m/s
V_{tip}	Rotor tip speed, $V_{tip} = \Omega R$, m/s
V_∞	Free stream velocity, m/s
x,y,z	Spatial coordinates, m
α_{local}	Local flow field angle, deg
α_S	Shaft tilt angle, deg
α_W	Fixed-wing pitch angle, deg
$\Delta\alpha_i$	Rotor-induced angle of attack change, deg
γ	Lock number
Γ_v	Vortex circulation, m^2/s
θ_0	Rotor root collective angle, deg
θ_{1c}	Rotor lateral cyclic control angle, deg
θ_{1s}	Rotor longitudinal cyclic control angle, deg
λ_2	Flow field operator, 1/s^2
μ	Advance ratio, $\mu = V_\infty/\Omega R$
ρ_∞	Freestream density, kg/m^3
σ	Rotor solidity, $\sigma = 4c_R/\pi R$
Ψ	Rotor azimuthal position, deg
ω_z	Vorticity component in z direction, 1/s
Ω	Rotor angular velocity, rad/s

Presented at 45th European Rotorcraft Forum, Warsaw, Poland, 17-20 September, 2019

1. INTRODUCTION

A recent doctrine in rotorcraft development is the pursuit of higher flight speeds without sacrificing hover capabilities or lowering overall vehicle performance. This extension of the flight envelope would benefit many mission scenarios such as medical emergency transport, search and rescue, and police operations. The maximum speed of conventional helicopters is limited by the onset of compressibility effects on the advancing rotor blade side [1]. These compressibility effects are characterized by shock-induced flow separation, resulting in increased levels of structural vibrations, blade drag, and power consumption. A typical approach to counter these effects is to slow down the main rotor [2], i.e. to operate it at a high advance ratio μ, defined as the ratio of flight speed V_∞ to rotor tip speed (ΩR), where Ω is the rotor rotational speed and R the rotor radius. The slowed rotor operation comes at the cost of reduced rotor thrust on the retreating blade side due to the occurrence of reverse flow [3-6]. This flow regime features flow from the sharp geometric trailing edge towards the blunt geometric leading edge of the airfoil and is characterized by flow separation, vortex shedding, and negative sectional blade lift [7]. For articulated rotors, the reduced lift in the reverse flow region results in reduced overall lift due to the required balance between the advancing and the poorly performing retreating rotor side, i.e., zero hub rolling moment [8]. Hingeless rotors, on the other hand, may not have to be trimmed to zero hub rolling moment and can therefore fully exploit the lift potential on the advancing blade side. Operation in this so-called “lift-offset” state requires changes in the overall rotorcraft configuration to ensure trimmed forward flight, e.g., by combining two counter-rotating rotors in coaxial configuration, as carried out in the Sikorsky X2 Technology™ demonstrator [6].

Another promising approach of realizing trimmed forward flight with a single lift-offset rotor is to add a fixed-wing on the retreating blade side of the rotorcraft that produces additional lift and counters the rolling moment of the rotor. Compared to a coaxial rotorcraft, this asymmetric configuration reduces the mechanical complexity of the rotor system and therefore potentially the production and operational cost of the aircraft. Installation of control surfaces on the fixed-wing can further add control redundancy to the aircraft, providing in-flight performance optimization capabilities and increased maneuverability. Sridharan et al. [9] and Jo and Choi [10] conducted comprehensive rotorcraft design studies of asymmetric lift-compound configurations and found that they exhibited similar or better performance than coaxial rotorcraft at high flight speeds. To date, however, no detailed CFD or systematic wind tunnel studies appear available, which demonstrate the benefits of asymmetric lift-compound configuration.

The focus of the present study is on experimentally characterizing the performance and demonstrating the feasibility of a lift compound helicopter with a hingeless rotor in conjunction with a single fixed-wing on the retreating blade side. The performance of rotor, wing, and compound vehicle is quantified with and without fixed-wing at advance ratios μ between 0.3 and 0.5, using slowed rotor speeds of 700 and 1200 RPM, and zero and aft (4 deg) shaft tilt angles. Optical flow field measurements are applied to study dominant aerodynamic interaction effects between the rotor and wing, as well as flow features present in the reverse flow regime.

2. EXPERIMENTAL SETUP

2.1. Test stand

The tests were conducted using a Mach-scaled rotor test stand [8] that was modified to test lift-compounding, as shown in Fig. 1. The test stand was converted from an articulated to a hingeless hub design by replacing the hinges with solid blade attachment blocks to enable non-zero hub rolling moments and the realization of lift-offset. The 4-bladed rotor had a radius of $R = 0.846$ m, chord length of $c_R = 80$ mm, and solidity of $\sigma = 4c_R/\pi R = 0.12$. The blades were untwisted with rectangular planform, root cutout of 16.4%R, and symmetric NACA0012 airfoil. The blades had a Lock number of $\gamma = 4.26$, mass per span of 0.321 kg/m, flap bending stiffness EI_y of 42.8 Nm^2, lag bending stiffness EI_x of 951.3 Nm^2, and torsional stiffness GJ of 26.5 Nm^2. The nominal rotor speed was 2300 RPM or $\Omega = 240.8$ rad/s for full Mach-scaling, but tests were conducted at slowed rotor conditions with 700 RPM ($\Omega = 73.3$ rad/s) and 1200 RPM ($\Omega = 125.7$ rad/s) to realize advance ratios of $\mu = V_\infty/\Omega R$ between 0.3 and 0.5. The first flap frequency was 1.66/rev for 700 RPM and 1.38/rev for 1200 RPM. The operating frequencies were chosen to avoid a resonance peak at 900 RPM, which had been determined by a dynamic calibration, as detailed in Ref. [11].

The test stand was equipped with a 5-component hub balance (three forces, pitching and rolling moment), strain gauged shaft torque cell, 3-component accelerometer to monitor test stand vibrations, two optical shaft encoders for RPM and blade azimuth measurements, and three Linear Variable Displacement Transducers (LVDT) for monitoring the control angles. Sensors in the rotating frame included Hall sensors to measure

Presented at 45th European Rotorcraft Forum, Warsaw, Poland, 17-20 September, 2019

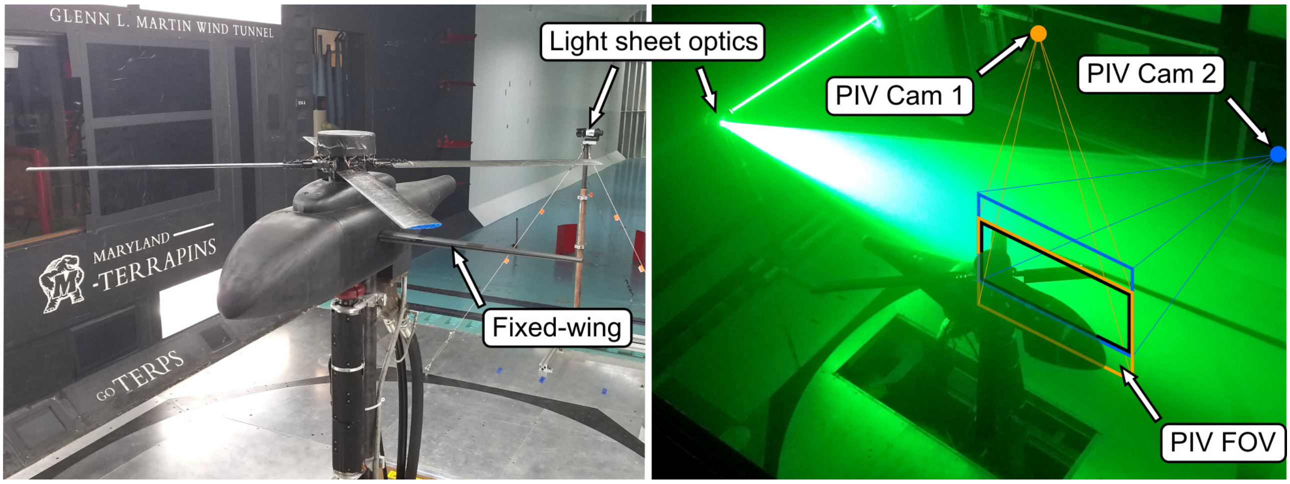

Fig. 1. Test setup in wind tunnel, showing hingeless rotor and fixed-wing (left) and PIV setup (right)

blade pitch, strain gauges to measure pitch link loads, and strain gauges at a radial station of 25%*R* on the blades for measuring flap (all blades) and lag bending (Blade 1 and 3), as well as torsional strain (Blade 2 and 4). A slip ring system with 150 lines transferred the signals from rotating frame to the test stand. All sensor signals were recorded with a National Instruments 16-bit analog-to-digital converter controlled by a Labview virtual instrument panel at a sampling rate of 5 kHz and over a total duration of 5 s.

A new modular fuselage was added to the test stand to enable the attachment of a fixed-wing and eventually a pusher propeller at the end of the tail. The fuselage was constructed based on a modified ROBIN fuselage [12] and scaled to match the rotor radius. The total height of the fuselage was increased by 10% to 0.301 m and the width by 19.7% to 0.254 m in order to contain a newly designed support structure for mounting the fixed-wing on the test stand. The length of the converging tail section was decreased by 9% and a semi-sphere added at the rear end, resulting in a total length of the fuselage of 1.475 m. The fuselage was manufactured using Fused-Deposition-Modeling with Stratasys ULTEM™ 9085 resin and attached to the test stand through a rigid steel and aluminum support structure and 14 vibration-damping mounts. Six removable lids were placed on either side of the fuselage to enable mounting of the fixed-wing at different vertical and longitudinal positions.

2.2. Fixed-wing

A fixed-wing was added to the test stand as shown in the left photograph of Fig. 1. The wing had a span of $b_W = 0.594$ m (70%*R*), aspect ratio of $AR = 5$, and taper ratio of 0.5, resulting in a chord length of $c_{root} = 0.158$ m, $c_{tip} = 0.079$ m, and $c_W = 0.142$ m at the location of the PIV light sheet. The wing had a NACA0015 airfoil at the wing tip and NACA0020 at the root to allow for rigid attachment to the test stand. The wing was manufactured using Fused-Deposition-Modeling with Stratasys ABS-M30 resin and had a tapered steel spar for support. A 6-component strain gauged load balance from NASA was implemented within the wing root to determine the fixed-wing loads, most importantly lift, drag, and rolling moment. The wing was installed on the retreating blade side of the fuselage at a height of $z_W = –24\%R$ below the rotor and $x_W = 0\%R$ behind the rotor hub with a fixed pitch angle of $\alpha_W = 8$ deg.

2.3. Optical flow measurement setup

The flow field between the fixed-wing and rotor on the retreating blade side was measured with a stereoscopic Particle Image Velocimetry (PIV) system to study interaction effects between the aerodynamic components, as well as flow features in the reverse flow domain. The system is shown on the right hand side of Fig. 1 and consisted of two Imager LX29M CCD cameras and a Quantel Evergreen PIV 200 Nd:YAG laser. The cameras had a resolution of 6600 × 4400 pixels and were equipped with Nikon Nikkor lenses with a focal length of 135 mm. The cameras were positioned outside the test section on the retreating blade side of the rotor at a lateral distance of 1.9 m to the rotor hub and 1.03 m upstream and 1.56 m downstream of it, with a corresponding stereo angle of 68 deg between the cameras, as shown on the right hand side of Fig. 1.

The beam of the PIV laser entered the test section through a breather slot and passed through light sheet optics located downstream of the model, as seen in the background of both photographs in Fig. 1. The optics formed a vertical light sheet that was oriented along the main flow direction and located at a lateral position of 30%R from the hub. The light sheet had a thickness of 2–3 mm in the region of interest and illuminated mineral oil particles distributed in the test section.

The field of views (FOV) of the two PIV cameras are sketched in the right hand photograph of Fig. 1 and both measured 600 mm × 370 mm. The downstream camera 1 was lowered by 120 mm compared to the upstream camera 2 in order to avoid strong reflections on the trailing edge of the fixed-wing. The resulting stereoscopic data with three velocity components (3C) in a reduced FOV of 600 mm × 250 mm size resolved the mutual interaction effects between the wing and rotor. In addition, the monoscopic, two velocity component (2C) data above the 3C-velocity field was used to study flow features in and above the rotor plane.

Particle images were recorded at phase-locked rotor blade positions between Ψ = 250 deg and Ψ = 290 deg rotor azimuth. Temporal synchronization was realized with a programmable timing unit from LaVision based on 1/rev and 60/rev trigger signals from the optical shaft encoders on the test stand. A total of 50 images were recorded per test condition, with one image being recorded every 7 rotations for 700 RPM rotor speed and every 12 rotations for 1200 RPM, due to the limited frame rate of the high-resolution cameras.
The recorded particle images were processed and phase-averaged with LaVision's Davis 10 software. A multi-grid cross-correlation algorithm was applied, starting at interrogation windows of 96 × 96 pixels and refined down to 32 × 32 pixels with window overlaps of 75%. The 50 vector fields corresponding to each test point were subsequently phase-averaged and masks were applied to regions affected by the laser shadow or by bright reflections in the background. The 2C and 3C velocity fields were post-processed with Matlab. Locations of the rotor blades and fixed-wing contour within the light sheet were extracted from the mapped measurement images. Tracking of vortices in the flow field was carried out based on the λ_2 criterion [13], according to the definition given in Ref. [14]. For the spatial coordinates (x,y,z) within the PIV plane in the longitudinal (x), vertical (y), and out-of-plane (z) direction and the corresponding velocity components (u,v,w), λ_2 is defined here as:

$$(1) \quad \lambda_2 = \frac{\left(\frac{\partial u}{\partial x}\right)^2 + \left(\frac{\partial v}{\partial y}\right)^2}{2} + \frac{\partial v}{\partial x}\frac{\partial u}{\partial y}$$

The vortex center positions were detected based on the area center (centroid) of the λ_2 field. Additionally, the rotational direction was used to distinguish vortices with different sign of rotation, such as blade tip vortices and reverse flow dynamic stall vortices. Vortex strength was quantified based on the tangential velocity component V_{swirl} around the detected vortex centers. For increased robustness and reduced susceptibility to outliers, the Vatistas vortex model [15] was fitted to the swirl velocity distribution:

$$(2) \quad V_{\mathrm{Vatistas}}\left(\frac{r}{r_c}\right) = \frac{\Gamma_v}{2\pi r_c} \frac{\frac{r}{r_c}}{\left(1+\left(\frac{r}{r_c}\right)^{2n}\right)^{\frac{1}{n}}}$$

where r is the radial distance from the vortex center, r_c is the core radius, Γ_v is the vortex circulation, and n is a fit factor which was chosen in the range of n=1 (Kaufmann-Scully vortex [16,17]) to n=2 (Bagai-Leishman vortex [18]). The peak value of the tangential velocity distribution $V_{\mathrm{swirl,max}}$ served as a measure for the strength of the vortex.

2.4. Comprehensive Analysis

Experimental data were correlated with predicted results obtained from the University of Maryland Advanced Rotorcraft Code (UMARC). The prediction tool has been previously validated against Mach-scaled wind tunnel data [19] and full-scale UH-60A test data [20]. UMARC uses a structural model that covers coupled elastic flap, lag, twist, and axial deformations up to second order non-linear terms. The blade structure and azimuthal range are resolved by a finite element method in space and time. The blade was discretized into 20 elements, each element consisted of 15 degrees of freedom to account for coupled flap, lag, axial, and torsional motion. The time domain was resolved into 12 elements with each consisting of 5th order polynomial. The computational speed was increased by applying modal reduction with up to 10 coupled modes. Blade aerodynamics are resolved based on the lifting-line theory and 2D airfoil look-up tables. The wake far from the blades was modeled by the Bagai-Leishman free-wake model [18] and the near wake up to 30 deg azimuth behind the rotor was modeled by the Weissinger-L representation [21]. Unsteady aerodynamics, such as dynamic stall, were accounted for by the Leishman-Beddoes model [22]. A semi-prescribed wind tunnel trim was employed, where the experimental collective angle is used and the cyclic controls were iterated to reach the trim target, which was achieved by zeroing hub moment for normal-trim cases and balancing the wing-induced rolling moment for the offset-trim and wing-trim cases. It should be noted that the analysis did not account for fuselage and fixed-wing effects.

Presented at 45th European Rotorcraft Forum, Warsaw, Poland, 17-20 September, 2019

The comprehensive analysis results were modified to take into account the effects of fixed-wing loads on vehicle performance. The modification was based on high-fidelity computational fluid dynamics (CFD) simulations of an isolated fixed-wing and a simple momentum theory approximation of the rotor-induced reduction of wing lift. The Reynolds-Averaged Navier Stokes (RANS) simulations were carried out with Ansys Fluent 19.2. The transition SST 4-equation turbulence model was used and the discretization method was a second order upwind scheme. The computational domain around the wing was hemispherical with a symmetry boundary condition at the wing root and was resolved with a hybrid grid of 8.9 million cells. Flow conditions were selected corresponding to the experimental conditions without rotor, with a wing angle of attack of $\alpha_W = 8$ deg and free-stream velocity ranging between $V_\infty = 18.7$ m/s and 42.5 m/s. The fixed-wing lift-to-drag ratio was extracted from the simulations for all flow conditions under investigation. To ensure that the lift-share ratio $LS = L_W / (L_R + L_W)$ of the model matched the experimental conditions, the comprehensive wing lift $L_{W,U}$ was determined based on the UMARC rotor lift and experimental lift-share ratio:

(3) $$L_{\mathrm{W,U}} = \frac{LS}{1-LS} L_{\mathrm{R,U}}$$

To further consider the effect of rotor downwash on wing lift, a correction of the effective angle of attack of the wing was applied based on momentum theory for forward flight conditions. In a first step, the vertical rotor-induced velocity in the rotor plane v_i was determined iteratively based on:

(4) $$v_{\mathrm{i}} = \frac{\frac{T}{2\rho_\infty A_{\mathrm{R}}}}{\sqrt{(V_\infty \cos\alpha_{\mathrm{S}})^2 + (V_\infty \sin\alpha_{\mathrm{S}} + v_{\mathrm{i}})^2}}$$

where A_R is the rotor disk area. At infinite downstream distance, the rotor-induced velocity reaches $2v_i$ due to wake contraction. At the fixed-wing location, the vertical induced velocity was slightly larger than v_i, but estimated as v_i here for repeatability. Together with the free-stream velocity V_∞ and neglecting the effect of the fixed-wing itself, the rotor-induced angle of attack increment $\Delta\alpha_i$ on the fixed-wing was calculated:

(5) $$\Delta\alpha_{\mathrm{i}} = \arctan(v_{\mathrm{i}}/V_\infty)$$

The modelled fixed-wing lift L_W was reduced based on a reduction of the effective angle of attack, assuming attached flow and wing operation within the linear lift curve slope:

(6) $$L_{\mathrm{W}} = \frac{\alpha_{\mathrm{W}} - \Delta\alpha_{\mathrm{i}}}{\mathrm{a_W}} \cdot L_{\mathrm{W,U}}$$

Finally, the corresponding fixed-wing drag was calculated based on the modelled fixed-wing lift and a second order regression of the CFD lift-to-drag ratio, taking into account the wing drag at zero angle of attack.

2.5. Test Procedure

The wind tunnel test consisted of multiple sweeps of the blade root collective between $\theta_0 = -2$ deg and $\theta_0 = 12$ deg for the rotor at advance ratios of $\mu = 0.3 - 0.5$ at 700 RPM and $\mu = 0.3 - 0.4$ at 1200 RPM, as well as rotor shaft tilt angles of $\alpha_S = 0$ deg and $\alpha_S = 4$ deg aft. All test conditions were repeated for three different trim conditions:

- **Normal-trim**, standard rotor trim without fixed-wing
- **Wing-trim**, lift-compound rotor trim with finite rolling moment M_x and fixed-wing present
- **Offset-trim**, rotor trim with rolling moment according to wing-trim, but without the fixed-wing

These conditions were selected to isolate the impact of added fixed-wing and rotor offset-trim on vehicle aerodynamics and performance. Additional reference test data was acquired for configurations without rotor blades, both with and without the fixed-wing. PIV images were recorded for collective pitch angles of $\theta_0 = 4$ deg and 10 deg for all test conditions.

3. RESULTS

The results are divided into five subsections, starting with a characterization of rotor performance for wing-trim conditions, as the normal-trim conditions have already been discussed in previous papers [11,19]. The mutual interaction effects of rotor and fixed-wing are discussed in sections 3.2 and 3.3, followed by a discussion of lift-compound vehicle performance in section 3.4, and analysis of the reverse flow field in section 3.5.

3.1. Rotor with wing-trim

Baseline rotor results are presented here for the hingeless rotor in lift-compound configuration with fixed-wing and wing-trim. Figure 2 shows trends for the vertical rotor thrust component (lift) L_R, torque Q, and cyclic trim angles θ_{1s} and θ_{1c} over collective θ_0 for different advance ratios μ at 700 RPM rotor speed (filled markers), as well as corresponding results from the comprehensive analysis UMARC

Presented at 45th European Rotorcraft Forum, Warsaw, Poland, 17-20 September, 2019

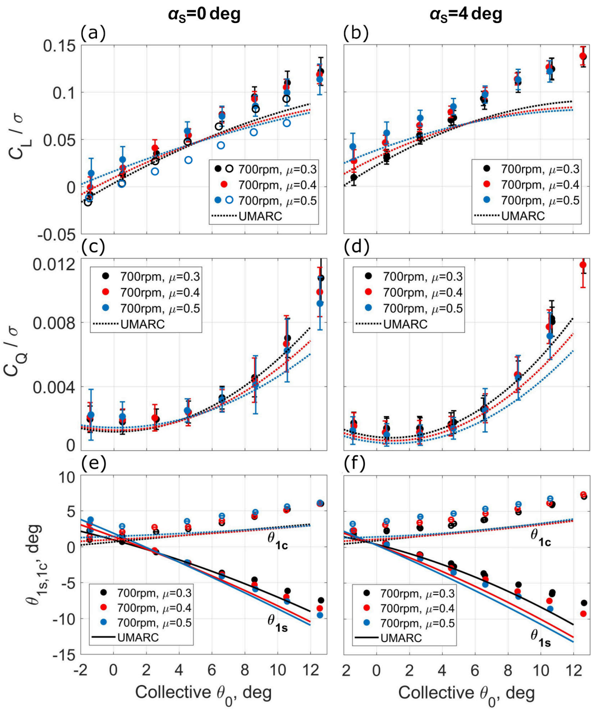

Fig. 2. Trends of rotor lift, torque, and cyclic pitch angles $\theta_{1s,c}$ over collective θ_0 for different shaft tilt α_S and wing-trim conditions.

(dotted lines). Data from Ref. [11] for a comparable rotor in normal-trim conditions is plotted in Fig. 2(a) for comparison (unfilled markers). Lift L_R and torque Q are both normalized with $\rho_\infty \pi R^2(\Omega R)^2$ and the rotor solidity σ, and plotted in the form of C_L/σ and C_Q/σ. The plots depict data for shaft tilt angles of $\alpha_S = 0$ deg in Fig. 2(a,c,e) and $\alpha_S = 4$ deg (aft tilt) in Fig. 2(b,d,f). Only results for the 700 RPM cases are shown, as the trends are comparable for the 1200 RPM test cases. The error bars in all graphs depict the standard deviation of the experimental values as a measure for the cycle-to-cycle variations. The standard deviation for the cyclic pitch angles is also added to the graphs, but too small to be visible.

The lift plots in Figs. 2(a) and 2(b) present a close-to-linear trend for small collectives and decreased slope with increasing advance ratio, similar to previously published articulated rotor results [23]. The slope changes are also predicted by UMARC, but lift is underpredicted for higher collective, more so at $\alpha_S = 4$ deg. The impact of normal- and wing-trim on lift is highlighted in Fig. 2(a) as the difference between the unfilled and filled markers. For an example collective of $\theta_0 = 10.6$ deg, lift is increased by up to $\Delta C_L/\sigma = 0.032$ (or +48%) for $\mu = 0.5$, due to the higher lift potential on the advancing side of the wing-trim rotor. In accordance with Ref. [23], aft shaft tilt is found to increase lift for all θ_0, with the most pronounced increases occurring at lower collectives, e.g. $\Delta C_L/\sigma = 0.03$ at $\theta_0 = -1.4$ deg for $\mu = 0.5$.

The shaft torque curves corresponding to the same wing-trim rotor are plotted in Fig. 2(c) and 2(d), respectively, for zero and 4 deg aft tilt. For collectives below $\theta_0 = 5$ deg, the measured torque is almost constant over collective and advance ratio at $C_Q/\sigma \approx 0.002$ (zero shaft tilt) and $C_Q/\sigma \approx 0.0014$ ($\alpha_S = 4$ deg). For higher collectives, torque steeply increases in a second order manner by a factor of 5–8 at $\theta_0 = 12.6$ deg. Aft shaft tilt of $\alpha_S = 4$ deg reduces shaft torque at low collectives $\theta_0 < 7$ deg, but increases it at higher collectives. Shaft torque is reduced with increasing advance ratio, e.g. by 15% between $\mu = 0.3$ and $\mu = 0.5$ at $\theta_0 = 12.6$ deg. The main driver for this is the increasing size of the reverse flow region, in which the chordwise blade loads are reversed. The general shaft torque trends with collective, advance ratio, and shaft tilt are adequately captured with UMARC.

Figures 2(e) and 2(f) show the cyclic control angles that are required for trimmed rotor operation in wing-trim configuration. Comparison between the two graphs shows that shaft tilt only has a marginal effect on the control angles. For increasing θ_0, the lateral control angle θ_{1c} has to be raised to about 5 deg and an increasingly negative longitudinal control angle θ_{1s} is required to counteract lift loss in the reverse flow region. The magnitude of both control angles increases slightly with increasing advance ratio. For the aft shaft tilt case in Fig. 2(f), the inflow condition is changed throughout the rotor disk, resulting in an increased angle of attack. Lift is correspondingly increased on the entire rotor plane with the exception of the reverse flow region, consequently requiring more negative longitudinal cyclic to counteract this imbalance. Compared to trim data for a normal-trim rotor case, as reported in Ref. [11], the present wing-trim case allows for a larger lift offset and therefore exhibits a reduced magnitude of the longitudinal cyclic. The UMARC results closely resemble the trend and advance ratio dependency of experimental control angles, but exhibit increasing deviation in magnitude for higher collectives and advance ratios. An offset of about -2 deg is found for the lateral control angles, which is in accordance with earlier results, such as in Ref. [23].

3.2. Effect of rotor on wing

Depending on the advance ratio, the fixed-wing is located completely (for small advance ratios) or partly (for intermediate advance ratios) in the wake of the rotor. The rotor operating conditions therefore have a substantial effect on the fixed-wing performance, which is characterized in this section based on load and flow field measurements. Figure 3 shows the lift of the fixed-wing L_W as a function of the collective angle θ_0 of the rotor blades for different advance ratios $\mu = (0.3, 0.4, 0.5)$, rotor speeds (700 RPM,

Presented at 45th European Rotorcraft Forum, Warsaw, Poland, 17-20 September, 2019

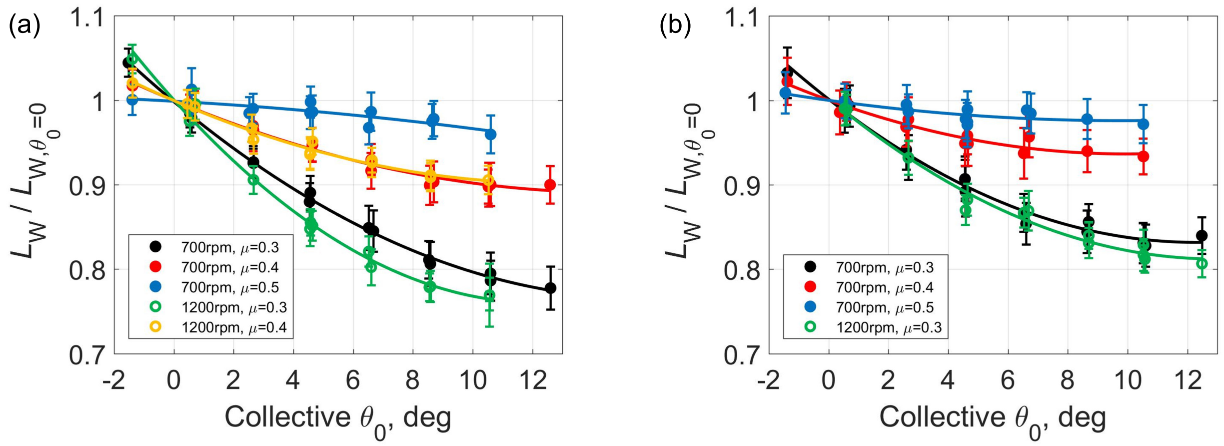

Fig. 3. Normalized wing lift over rotor collective for different μ and rotor speed (a) $\alpha_S = 0$ deg, (b) $\alpha_S = 4$ deg

1200 RPM), and shaft tilt angles (Fig. 3a: $\alpha_S = 0$ deg, Fig. 3b: $\alpha_S = 4$ deg). The wing lift is normalized with the wing lift at zero rotor collective, represented by the intersection point of the individual curves at $\theta_0 = 0$ deg. The markers represent actual measurement points and quadratic regression curves are added as a guide to approximate trends. All depicted curves show a decrease in wing lift with increasing rotor collective and the corresponding increase in rotor thrust. This effect is more pronounced at lower advance ratios and lower rotor speed, as evident when comparing the lift reduction at $\theta_0 = 10.6$ deg collective compared to the zero thrust condition. At this collective, lift is reduced by 4% for $\mu = 0.5$ at 700 RPM, 21% for $\mu = 0.3$ at 700 RPM, and 23% for $\mu = 0.3$ at 1200 RPM. These reductions are correlated with the estimated rotor-induced angle of attack change $\Delta\alpha_i$ at the fixed-wing location. The vertical rotor-induced velocity in the rotor plane v_i is estimated using momentum theory, as previously described in section 2.4 and Eqs. (4) and (5). The calculation is based on experimental measurement values and assumes fast forward flight, i.e., $V_\infty >> v_i$. Together with the free-stream velocity V_∞ and neglecting the effect of the fixed-wing itself, the rotor-induced angle of attack increment is calculated. Table 1 presents the resulting rotor-induced angle of attack increments $\Delta\alpha_i$ for a rotor collective of $\theta_0 = 10.6$ deg and shaft tilt of $\alpha_S = 0$ deg. The estimated values of $\Delta\alpha_i$ are inversely proportional to advance ratio and exhibit negligible dependence on rotor speed. The reduction in fixed-wing lift correlates well with $\Delta\alpha_i$ and is caused by the reduced effective angle of attack of the wing due to the induced downwash from the rotor. It is noted that the present simple approximation of $\Delta\alpha_i$ over-predicts lift reduction, but correlates well qualitatively. For aft shaft tilt (Fig. 3b), a similar trend is found as for $\alpha_S = 0$ deg, but the impact of rotor downwash on fixed-wing lift is slightly reduced.

Table 1. Rotor-induced angle of attack change for $\theta_0 = 10.6$ deg rotor collective and $\alpha_S = 0$ deg

μ	0.3	0.3	0.4	0.4	0.5
RPM	700	1200	700	1200	700
V_∞, m/s	19	32.3	25	42.5	31
v_i, m/s	1.3	2.1	1	1.6	0.7
$\Delta\alpha_i$, deg	3.9	3.7	2.3	2.2	1.4

Changes in local flow field angle $\alpha_{local} = \tan^{-1}(v/u)$ due to the rotor downwash are also quantified based on PIV measurements at the 30%R lateral location. Fig. 4 depicts measurements of α_{local} at three distinct vertical positions ($y/c_W = 0.2$, 0.6, 1.0) in the region between fixed-wing ($y/c_W = 0$) and rotor plane ($y/c_W = 1.4$) for different advance ratios, shaft tilt angles, and cases with and without fixed-wing. The local flow field angle is averaged over 10 horizontal rows of velocity vectors (height of 5%c_W) and plotted along the longitudinal x coordinate. Each subplot contains 3 to 5 color-coded α_{local} plots for different rotor blade azimuthal positions Ψ_{blade} between 250 deg and 290 deg (vertical plot axes). The color map of the graphs is cut off at $\alpha_{local} = \pm 3$ deg and shown in the top left corner of Fig. 4. The phase-resolved data allows for a separation of flow features that are caused by the fixed-wing and hence stationary, or by the moving rotor blade. The leading edge of the fixed-wing is located at $x/c_W = 0$ and the trailing edge at $x/c_W = 1$, as marked by black vertical lines in each subplot. It should be noted that only data for 700 RPM rotor speed is plotted here, as the flow fields for constant advance ratio and different rotor speed are indistinguishable, highlighting that the advance ratio is the dominant factor for the flow field angles. At the lowest vertical position of $y/c_W = 0.2$ close to the fixed-wing, the flow field is mostly steady and independent of rotor blade position, highlighting the dominance of the adjacent wing. Farther above the wing, the rotor downwash becomes increasingly dominant, as visible by the horizontal movement of

Presented at 45th European Rotorcraft Forum, Warsaw, Poland, 17-20 September, 2019

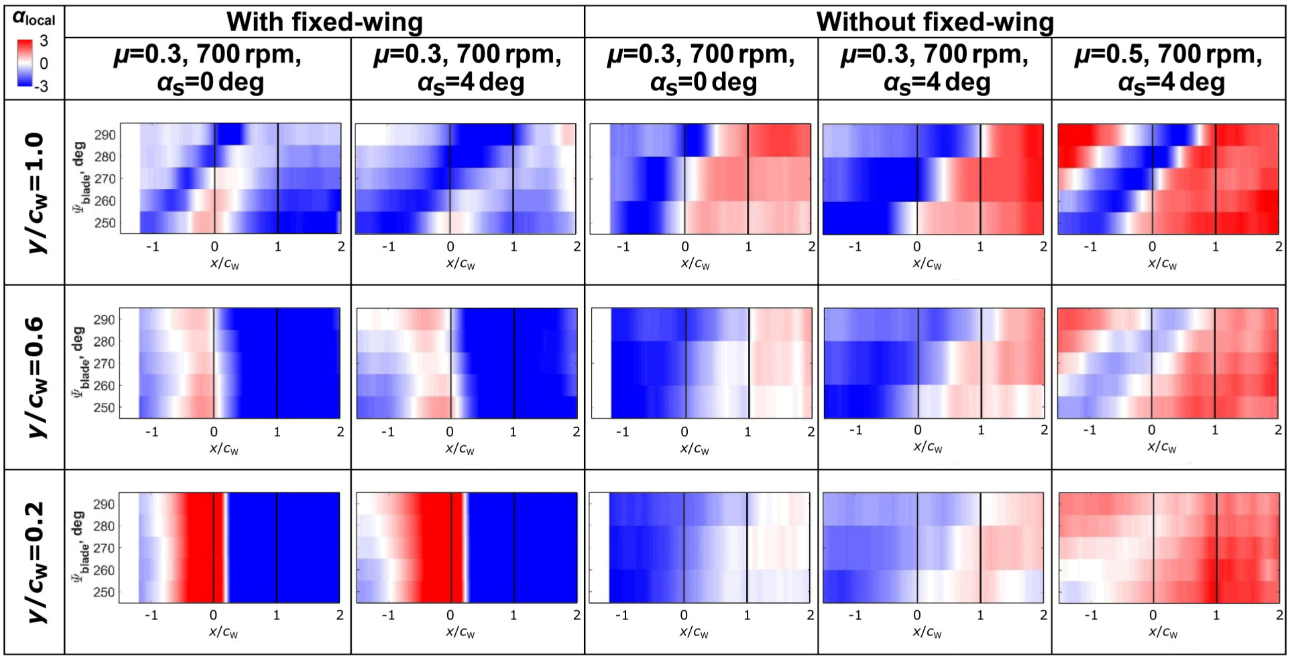

Fig. 4. Local flow field angle α_{local} at different heights y / c_W above fixed-wing for different advance ratio, shaft tilt, and with and without wing.

flow structures with varying blade azimuthal position. The presence of the rotor blade manifests as a local reduction in flow field angle with varying magnitude depending on the test conditions. Cases with and without aft shaft tilt show a similar flow field and dependency on the blade position, as visible in the two left columns of subplots in Fig. 4.

The three right columns in Fig. 4 depict the flow field without the wing, but with the rotor in offset-trim condition. At the uppermost position of $y / c_W = 1.0$, the absence of the fixed-wing is mostly notable downstream of the wing, with consistently larger flow field angles than for the fixed-wing case. The flow field upstream of the wing is more comparable to the fixed-wing cases, but the magnitude of the blade-induced variation in flow

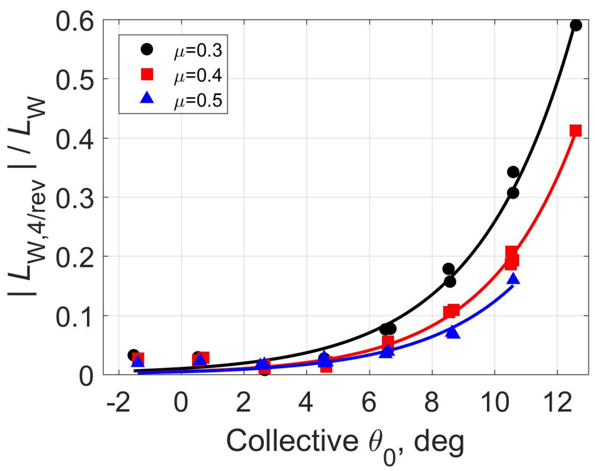

Fig. 5. Normalized 4/rev wing lift magnitude over rotor collective for range of μ at 700 RPM and $\alpha_S = 0$ deg

field angle increases with advance ratio. The rotor wake effect is also visible down to $y / c_W = 0.2$ for the cases without fixed-wing. This again manifests as a dependency of flow structures on blade azimuthal position. The influence of the rotor wake is especially visible for the rightmost column at $\mu = 0.5$, where the trace of the moving rotor blade appears at all three vertical positions and only varies in signal magnitude.

The effect of rotor downwash on the fixed-wing is further examined in terms of higher-harmonic wing loading in Fig. 5. The graph depicts the amplitude of 4/rev wing lift $|L_{W,4/rev}|$ normalized with mean wing lift L_W over rotor collective θ_0 for 700 RPM rotor speed, zero shaft tilt angle, and three different advance ratios. The 4/rev frequency corresponds to the blade passage frequency and isolates the blade effects from other lift fluctuations. The data points in Fig. 5 represent experimental measured values and are fitted with exponential functions of type $f(\theta_0) = a_1 \exp(a_2 \theta_0)$ to approximate trends. For low rotor collective $\theta_0 < 6$ deg, the 4/rev vibratory load of the fixed-wing exhibits negligible amplitudes below 3% of the mean lift for all studied advance ratios. The vibratory loads rapidly increase with higher rotor collective, reaching values of up to 59% of the mean lift for $\theta_0 = 12.6$ deg and $\mu = 0.3$. Vibratory loads are found to decrease with increasing advance ratio, similar to previous observations based on the data presented in Fig. 3. The 4/rev vibratory wing loads clearly illustrate the impact of the rotor-induced flow field on the fixed-wing and its dependence on advance ratio and rotor collective.

Presented at 45th European Rotorcraft Forum, Warsaw, Poland, 17-20 September, 2019

3.3. Effect of wing on rotor

With addition of the fixed-wing, the requirement of lateral balance of the rotor lift distribution is removed. The consequent changes in rotor lift and torque are examined, together with an analysis of the wing-induced flow field close to the rotor plane. Figure 6 depicts the effects of hub rolling moment trim, rotor shaft tilt angle α_S, and presence of the fixed-wing on rotor performance for a representative 700 RPM and $\mu = 0.4$ test case. The left subplot shows the rotor lift coefficient C_L normalized by rotor solidity σ over rotor collective θ_0. The right subplot contains the corresponding C_L / σ over torque coefficient C_Q / σ diagram. The five color-coded curves represent different combinations of shaft tilt α_S, wing presence, and rolling moment trim, according to the common legend in the right subplot. The error bars in both graphs depict the standard deviation of the experimental values as a measure for the cycle-to-cycle variations.

The bottom most lift curve (-●-) serves as a baseline case and corresponds to a conventional rotor test condition with zero shaft tilt, no fixed-wing, and zero hub moment trim and is comparable to previous wind tunnel tests such as [24]. For an example collective of $\theta_0 = 6$ deg, a lift coefficient of $C_L / \sigma = 0.058$ is obtained. In the second test case (-●-) the rotor is trimmed to the finite rolling moment that would be required to obtain vehicle trim around the longitudinal axis if a fixed-wing were present (offset-trim). This wing-free case is introduced to separate the contributions of non-zero rotor moment trim from the trimmed test case including a fixed-wing (-●-). The wing-free condition results in 17% increased rotor lift relative to the baseline case, whereas the trimmed wing condition increases rotor lift by 24% at $\theta_0 = 6$ deg. The corresponding lift/torque diagram shows that this increase in rotor lift does not change the rotor torque and that the curves for non-zero rolling moment trim with and without wing are highly comparable. As shown in previous studies [23], tilting the rotor shaft aft by $\alpha_S = 4$ deg (-●-) also increases rotor lift (+39% compared to baseline at $\theta_0 = 6$ deg), while simultaneously reducing required rotor torque (–21% at $\theta_0 = 6$ deg). The combination of aft shaft tilt with a trimmed fixed-wing (-●-) leads to lift improvements of up to 78% compared to the baseline case, with comparable rotor torque as for the baseline case. This dataset demonstrates the benefits of combining aft shaft tilt with a trimmed single fixed-wing configuration for increasing rotor lift without rotor torque penalty. It is noted that these benefits in rotor thrust do not take into account the lift produced by the fixed-wing, which further increases overall vehicle performance, as will be shown in the next section.

Figure 7 explores the effect of fixed-wing on the flow field around the rotor blades for different operating conditions. The three subplots contain local flow field angles α_{local} along a horizontal line at the 30%R lateral position and at $y / c_W = 1.2$, directly below the rotor plane at $y / c_W = 1.44$. The vertical distance to the rotor plane was selected to insure that the blade trailing edge and consequent laser shadow did not interfere with the measurements for any of the flow conditions studied. The longitudinal position x is normalized with the fixed-wing chord c_W, with $x / c_W = 0$ corresponding to the leading edge and $x / c_W = 1$ to the trailing edge of the wing, respectively. Figure 7(a) corresponds to a setup without rotor and without fixed-wing and Fig. 7(b) represents without rotor but fixed-wing. Figure 7(c) shows cases with a rotor in wing-trim condition with and without fixed-wing. The results are spatially averaged across five horizontal rows of velocity vectors. The plotted data corresponds to a fixed-wing angle of attack of 8 deg, rotor collective angle of $\theta_0 = 10.6$ deg, and rotor azimuth of 270 deg. The curves in Figs. 7(a) and 7(b) correspond to different wind tunnel and rotor shaft speeds, corresponding

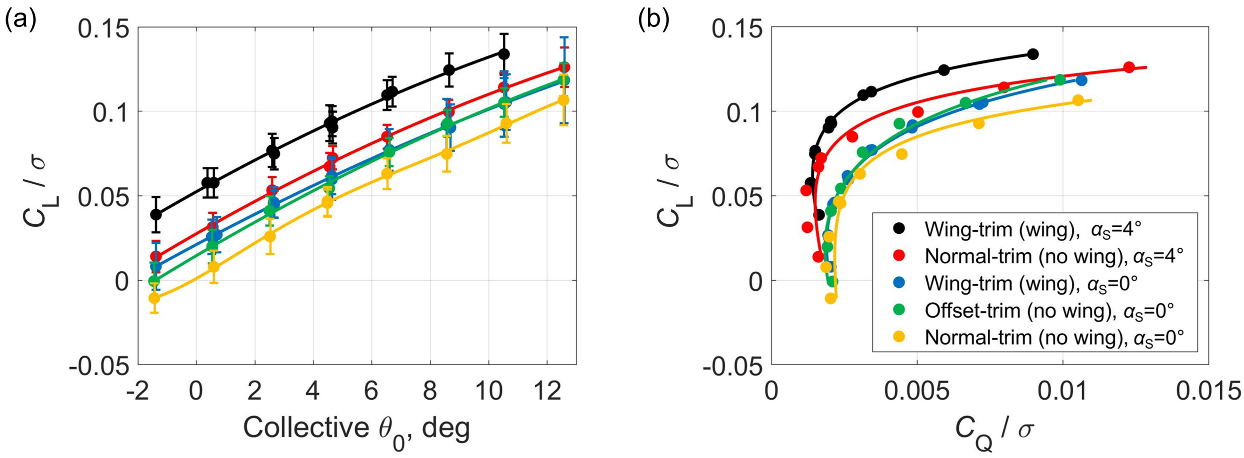

Fig. 6. Effect of shaft tilt α_S, fixed-wing, and rotor hub moment trim on rotor performance at 700 RPM and $\mu = 0.4$

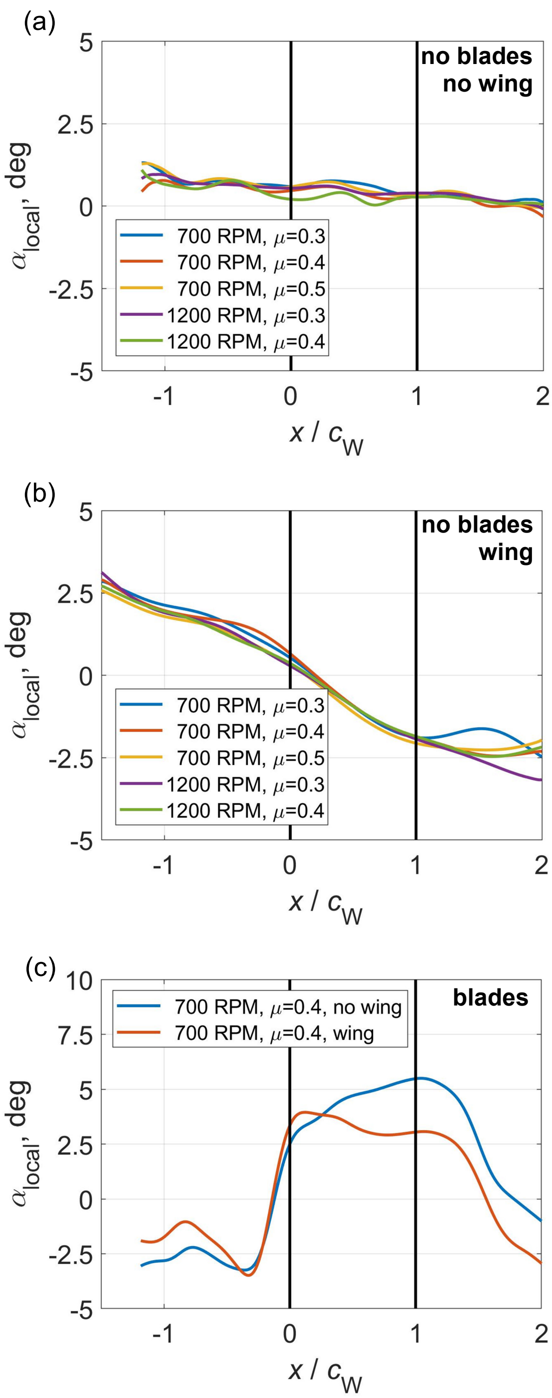

Fig. 7. Effect of wing on local flow field angle at $Y/c = 1.2$ close to rotor plane. (a) no wing, no blades, (b) wing, no blades, (c) blades at $\Psi = 270$ deg with and without wing.

to the previously presented rotor cases. For a better comparison, the corresponding legend entries are given in terms of rotor speed and a virtual advance ratio the fully-bladed rotor would have at these operating conditions.

The overlap of different curves in Figs. 7(a) and 7(b) illustrates that wind tunnel speed has a negligible influence on the local flow field angle at the measurement location close to the rotor plane.

For the reference case without rotor blades or fixed-wing, the local flow field angle varies between $\alpha_{local} = 1$ deg upstream and 0 deg downstream of the fixed-wing position. This change is attributed to the presence of the fuselage, which is located 15%R from the PIV measurement plane and induces an upward flow component upstream of the wing location. The added fixed-wing in Fig. 7(b) causes upwash upstream and downwash downstream of the fixed-wing quarter chord position at $x/c_W = 0.25$ with an amplitude of $\alpha_{local} = \pm 2.5$ deg. The qualitative angle of attack distribution is comparable to the effect of a single bound vortex at the fixed-wing location. Figure 7(c) presents the flow field angles just below the retreating rotor blade for cases with and without fixed-wing. For the test condition at $\mu = 0.4$ advance ratio, the flow field at the 30%R lateral location exhibits reverse flow, which is indicated by a reverse flow vortex at the trailing edge of the rotor blade at $x/c_W = -0.2$. The main difference between the two curves in Fig. 7(c) is found for $x/c_W > 0.25$, where the presence of the fixed-wing reduces the flow field angle by about 2 deg. This negative lift increment closely resembles the difference between Fig. 7(a) and 7(b) downstream of the wing. The upstream flow field is dominated by the reverse flow vortex and exhibits a slight wing-induced increase in the local flow field angle of about 1 deg, which is about half the size of the changes observed in the blade-free data. It is found that a simple linear superposition of the previous cases can partially predict the flow field for the wing-trim rotor case with fixed-wing, but breaks down in the vicinity of strong local vortices such as the reverse flow vortex. In terms of integral loads and the local flow field, the fixed-wing has a smaller effect on the rotor than that of rotor on the wing. This might change for a fixed-wing position closer to the rotor plane, where the presence of the fixed-wing increasingly resembles a partial ground effect of the rotor and significantly alters the flow field and load distribution of the rotor.

3.4. Overall aircraft performance

To assess the potential benefits and penalties of the lift-compound configuration with a single fixed-wing, overall performance variables such as lift-to-drag, required shaft torque, and required rotor collective for a specific total vehicle lift are presented in this section. Figure 8 presents effective lift-to-drag values over rotor collective θ_0 for different operating and trim conditions. Effective lift-to-drag is evaluated in the form of rotor lift L_R divided by effective rotor drag D_e:

$$\frac{L_R}{D_e} = \frac{L_R}{D_R + \frac{Q \cdot \Omega}{V_\infty}} \tag{7}$$

Presented at 45th European Rotorcraft Forum, Warsaw, Poland, 17-20 September, 2019

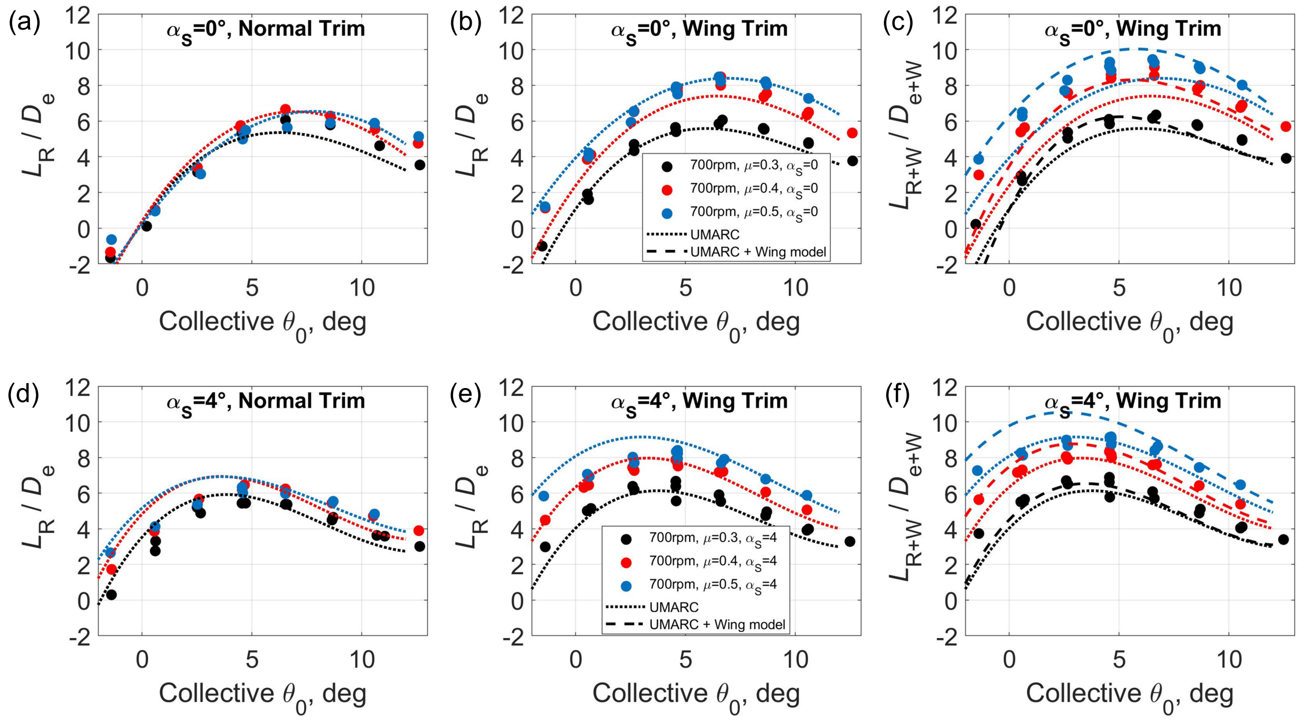

Fig. 8. Lift-to-drag ratio over rotor collective for (a-c) $\alpha_S = 0$ deg and (d-f) $\alpha_S = 4$ deg. Rotor in (a,d) normal-trim, (b,e) wing-trim, and (c,f) wing-trim plus wing load contributions

whereas the overall compound performance is evaluated based on the ratio of total lift to total drag:

$$\frac{L_{R+W}}{D_{e+W}} = \frac{L_R + L_W}{D_e + D_W} \tag{8}$$

The symbols in Fig. 8 represent test data for 700 RPM rotor speed and advance ratios of $\mu = 0.3$ (●), $\mu = 0.4$ (●), and $\mu = 0.5$ (●), as well as corresponding comprehensive code results (dotted lines). Figure 8(a-c) correspond to zero shaft tilt and Fig. 8(d-f) to aft shaft tilt of 4 deg. For normal trim and $\alpha_S = 0$ deg (Fig. 8a), a maximum lift-to-drag ratio of 6.65 is reached for $\mu = 0.4$ and $\theta_0 = 6.6$ deg. For smaller collectives, the three data sets converge towards zero at $\theta_0 = 0$ deg, while at larger collectives, lift-to-drag increases with advance ratio. Results of the comprehensive analysis closely match the experimental data, especially for larger collectives.

Figure 8(b) corresponds to the full compound configuration under wing-trim condition, but without wing loads. This intermediate step allows for a separate assessment of trim-induced performance changes without considering the extra loads of the fixed-wing. The optimum is again at $\theta_0 = 6.6$ deg, but increased dependency on advance ratio is found, with peak L_R / D_e values of 8.47 for $\mu = 0.5$ and 6.06 for $\mu = 0.3$. As mentioned before, the increase in rotor performance is due to the rotor's ability to produce additional lift on the advancing blade side. This effect is more pronounced for higher advance ratios – and consequently higher wind tunnel speed for constant rotor speed – due to the increases in dynamic pressure and rolling moment produced by the fixed-wing to counter increased rotor lift on the advancing blade side. For the investigated advance ratios, this lift increase on the advancing blade side surpasses lift reduction in the expanding reverse flow regime. As for the normal trim cases, the comprehensive analysis results closely follow experimental values, both in general trend and magnitude.

Figure 8(c) shows the total lift-to-drag ratios for the lift-compound vehicle, taking into account both rotor and fixed-wing loads, as specified in Eq. (8). The overall vehicle performance improves for all advance ratios and rotor collectives. Direct comparison of Fig. 8(b) and 8(c) shows that the improvement is maximal for $\mu = 0.5$ with an increase in lift-to-drag by 12% to 8.47, while values for $\mu = 0.3$ exhibit only marginal improvement. The largest performance increase occurs at lower collective angles or higher lift share factors, where the rotor has a suboptimal lift-to-drag ratio and the fixed-wing is affected less by the rotor downwash. The graph further features two sets of comprehensive rotor results. The dotted lines correspond to the same UMARC results as shown in Fig. 8(b), which do not take into account the

Presented at 45th European Rotorcraft Forum, Warsaw, Poland, 17-20 September, 2019

Table 2. Rotor-induced angle of attack change for $\theta_0 = 10$ deg and 700 RPM computed with UMARC

μ	0.3	0.4	0.5	0.3	0.4	0.5
α_S, deg	0	0	0	4	4	4
V_∞, m/s	18.7	24.9	31.2	18.7	24.9	31.2
v_i, m/s	0.99	0.70	0.54	1.08	0.77	0.58
$\Delta\alpha_i$, deg	3.03	1.61	0.99	3.31	1.78	1.07

Table 3. Changes of total vehicle L_{R+W}/D_{e+W} due to added fixed-wing and wing-trim

	$\mu = 0.3$	$\mu = 0.4$	$\mu = 0.5$
$\alpha_S = 0$ deg	+5%	+36%	+61%
$\alpha_S = 4$ deg	+27%	+29%	+45%

fixed-wing loads. In an attempt to augment the comprehensive rotor results, a simple wing load prediction is employed based on high-fidelity analysis of the fixed-wing without rotor and momentum theory, as described in section 2.4. Example results for the corresponding rotor-induced reduction of fixed-wing lift are given in Table 2 for a single collective angle of $\theta_0 = 10$ deg. The table presents the difference in induced angle of attack between different operating conditions, varying between $\Delta\alpha_i = 1$ deg and 3.3 deg. The augmented comprehensive model results exhibit improved correlation with experimental data compared to the standard UMARC results, with the best fit occurring at lower advance ratios and positive collective angles.

The lower half of Fig. 8 contains corresponding performance results for $\alpha_S = 4$ deg aft shaft tilt. Compared to $\alpha_S = 0$ deg, the peak lift-to-drag ratio is comparable, but occurs at smaller rotor collectives of about 2 – 4 deg, depending on advance ratio and trim condition. The comprehensive analysis captures the shift of peak performance towards lower rotor collectives and correlates well with experimental data for $\mu = 0.3 – 0.4$, but overpredicts L/D for $\mu = 0.5$ at all trim conditions. This overprediction also affects the augmented model in Fig. 8(f), with predicted lift-to-drag values up to 20% above the experimental data.

A summary of the increase in peak vehicle L/D relative to the normal-trim case (Fig. 8a) is given in Table 3 for different advance ratios and shaft tilt angles. The table shows that L/D increases by up to 61% ($\alpha_S = 0$ deg) and 45% ($\alpha_S = 4$ deg) at $\mu = 0.5$ if fixed-wing and wing-trim are considered.

Rotorcraft performance for different vehicle configurations is typically assessed with regard to certain mission scenarios. In the present study, a fixed total vehicle lift of 133 N (30 lb) is used to compare different levels of lift share between rotor and fixed-wing. This lift value was selected as it could be achieved for all tested advance ratios and lift share factors LS. Figure 9 depicts experimental values for the rotor collective θ_0 required to achieve a total vehicle lift of 133 N (Fig. 9a) and the resulting total lift-to-drag ratio L_{R+W}/D_{e+W} (Fig. 9b) for different lift share values. A lift share value of 0% corresponds to a conventional helicopter without fixed-wing. The symbols in both subfigures correspond to experimental data, while the exponential curves are added as a guide to approximate trends. The collective diagram contains two datasets for zero and aft shaft tilt at 700 RPM rotor speed. Both curves exhibit a reduction of required collective with increasing lift share. The zero shaft tilt requires consistently higher rotor collective ($\Delta\theta_0 = 2 – 6$ deg) to achieve the required total vehicle lift. At a maximum studied lift share of $LS = 23\%$, the required rotor collective is reduced by about 20% for $\alpha_S = 0$ deg and 64% for $\alpha_S = 4$ deg with respect to the conventional rotor configuration. The results thus show the benefits of aft shaft tilt and lift share for reducing required rotor collective at a fixed total lift condition.

Figure 9(b) shows corresponding total lift-to-drag values over lift share for different advance ratios (marked by color in the plot) and shaft tilt (solid and dashed lines). For a low advance ratio of $\mu = 0.3$, a

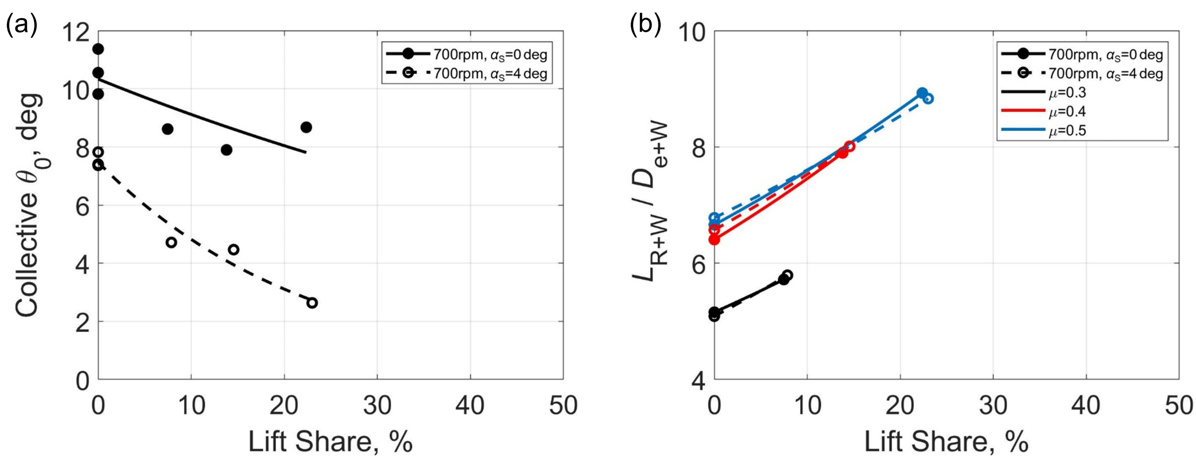

Fig. 9. Required rotor collective and corresponding L/D for different lift share values and 133 N total vehicle lift

Presented at 45th European Rotorcraft Forum, Warsaw, Poland, 17-20 September, 2019

reduced lift-to-drag ratio is found compared to the higher advance ratios, likely due to the decreased performance of the fixed-wing due to the rotor downwash, as shown in Fig. 3. A positive correlation between lift share and lift-to-drag ratio is observed. For the $\mu = 0.5$ case, a lift share value of 23% leads to noticeable improvement in overall lift-to-drag ratio from 6.7 to 8.9. The slopes of plotted curves are comparable and indicate that similar improvements are feasible for lower advance ratios as well, although different peak lift share values were realized for different advance ratios in this study. The effect of shaft tilt on overall vehicle lift-to-drag is found to be marginal across the entire range of investigated lift share values. It is noted that the current analysis does cover hover performance, where the fixed-wing might have detrimental effects on vehicle roll trim.

The analysis so far has neglected drag and other performance losses due to stabilizer and tail rotor required for yaw trim. This yaw trim is required to compensate for main rotor torque on both conventional and compound helicopters and is often excluded in wind tunnel tests [11,25]. A comparison between the conventional rotor configuration under normal-trim conditions (NT) and single wing compound configuration under wing-trim (WT) is shown in Fig. 10. The left-hand side graph depicts total torque coefficient $C_{Q,\mathrm{total}}$ divided by rotor solidity σ and plotted over rotor collective, comparable to Figs. 2(c) and 2(d). The symbols represent experimental data and third order polynomial curves are added as a guide to approximate trends. The filled markers and solid lines represent the conventional rotor under NT, while unfilled markers and dashed lines represent the lift-compound configuration including torque from both the rotor and fixed-wing. Figure 10(b) depicts the corresponding relative change in torque between standard configuration and lift-compound, averaged over the entire collective range.

Figure 10(a) shows that the aft shaft tilt increases shaft torque at collectives above 7 deg and reduces it at collectives below, independent of μ and trim condition. For $\mu = 0.5$, the added wing and wing-trim lead to a reduction of total torque of 17% – 28%. This reduction is smaller for lower advance ratios and almost zero for $\mu = 0.3$, where torque is even slightly increased for larger collectives. Figure 10 illustrates that fixed-wing drag helps compensate part of the rotor torque, thereby reducing required yaw moment for trimmed forward flight under most test conditions. Together with improved vehicle lift-to-drag, these findings demonstrate the potential performance benefits of a single fixed-wing compound configuration compared to a regular helicopter. It is noted here that the present study did not take into account thrust-compounding, which is required for the present aft shaft tilt cases. Future tasks in this research project involve an auxiliary propulsor on the test stand and will give a more comprehensive picture of the total performance of this rotorcraft configuration.

3.5. Reverse flow field analysis

Extracted flow velocities and local flow field angles have already been presented in Figs. 4 and 7 as part of evaluating the mutual aerodynamic effects of fixed-wing and rotor. The focus of this section is on analyzing flow phenomena such as reverse flow and blade tip vortices that are present in the flow field on the retreating blade side at 30%R lateral location. It was found that the topological features in the flow fields scale properly with advance ratio and exhibit marginal dependency of rotor speed. Hence, the present evaluation mostly focuses on flow cases recorded at 700 RPM.

Figure 11 depicts two phase-averaged example flow fields; a two-component result based on camera 2 in Fig. 11(a) and a three-component stereoscopic result based on both PIV cameras in Fig. 11(b), which has a reduced vertical extent.

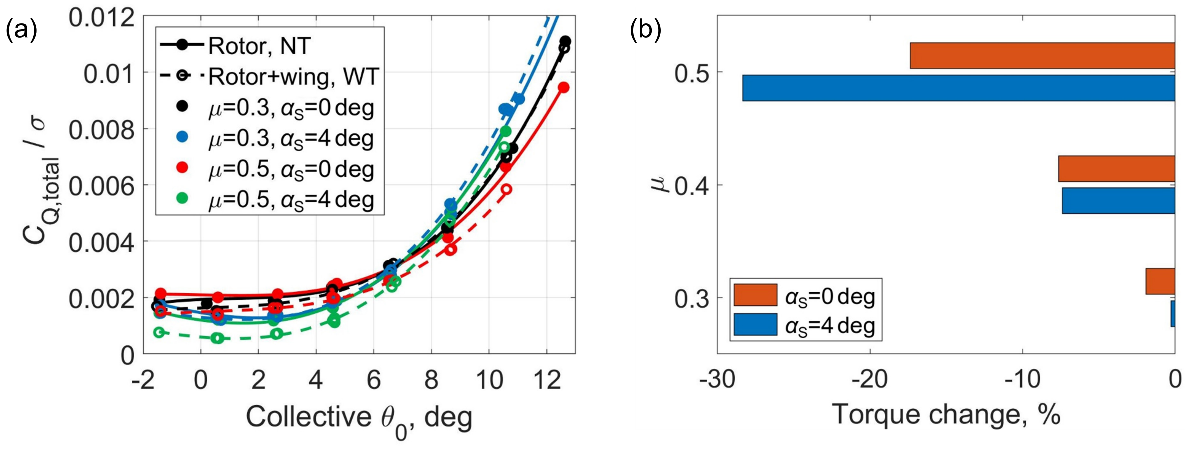

Fig. 10. Comparison of torque for single rotor in normal-trim (NT) versus rotor and fixed-wing in wing-trim (WT) (a) torque over collective and (b) average torque change for different shaft tilt and advance ratio

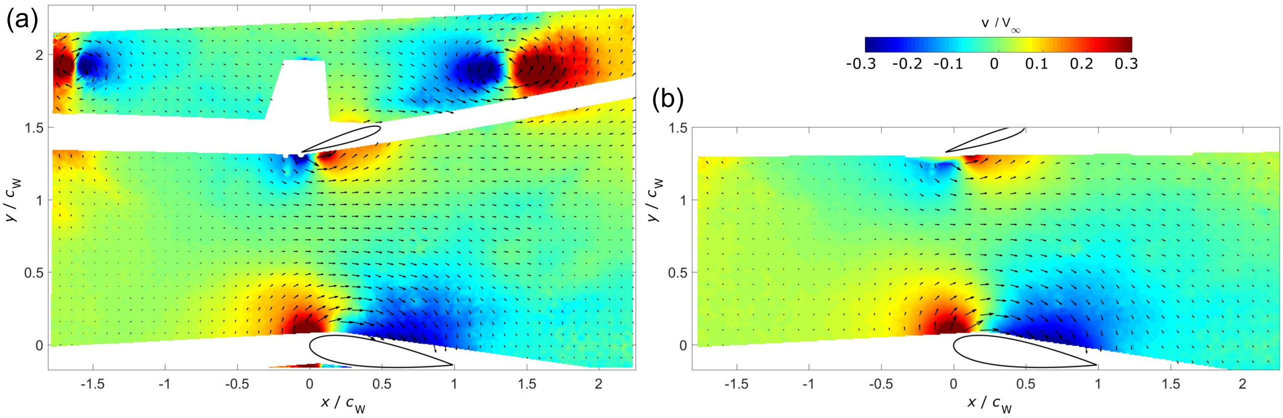

Fig. 11. Example 2- (a) and 3-component (b) PIV results, depicting contour plot of vertical velocity component v and down-sampled vector field ($u - V_\infty$, v) for $\mu = 0.5$, $\theta_0 = 10.6$ deg, $\alpha_S = 4$ deg, and $\Psi = 270$ deg rotor azimuth

The flow field depicted in both graphs corresponds to wing-trim conditions at an advance ratio of $\mu = 0.5$, collective $\theta_0 = 10.6$ deg, shaft tilt $\alpha_S = 4$ deg, rotor blade azimuth of $\Psi = 270$ deg, and rotor thrust coefficient of $C_T / \sigma = 0.1232$. Both plots show contour plots of the vertical flow component normalized with freestream velocity, v / V_∞, as well as the down-sampled in-plane velocity vector field ($u - V_\infty$, v) with one in 256 vectors shown. The positions of fixed-wing and rotor blade within the measurement domain have been extracted from the PIV images and are sketched in the plots. The laser light sheet optics were located downstream of the rotor test stand and laser shadows are present in the flow field, indicated by white areas to the left of the two airfoils. White areas on the right side of the two airfoils correspond to parts of the wing or rotor blade obstructing one or both of the camera views. The white area above the blade airfoil in Fig. 11(a) was masked due to the presence of bright reflections on the rotating rotor hub cap due to its proximity to the laser light sheet.

The part of the flow field between rotor and fixed-wing only exhibits small differences between the two subfigures, such as slight differences in vector spacing due to the image registration of the stereoscopic calibration. Quantitative comparison between the processed two- and three-component data found differences in in-plane velocity magnitude of <2% V_∞ in the region above the fixed-wing, where the impact of out-of-plane particle motion is greatest. Based on this comparison, the evaluation of vortex positions and strength in the remainder of this paper is based on two-component velocity fields recorded by camera 2.

The area above and below the rotor plane features multiple vortical structures, as visible in Fig. 11(a) in the form of circular streamlines and adjacent peaks of positive and negative vertical velocity component. The vortex at the left image border above the rotor plane with clockwise sense of rotation is a blade tip vortex that was created by a rotor blade in the forward part of the rotor plane and has convected downstream to its present location. The vortex below the rotor blade forms when the rotor blade experiences reverse flow on the retreating blade side and is called a reverse flow dynamic stall vortex [26]. It forms when flow separates at the sharp edge of the blade and the resulting shear layer rolls up into a vortex. This vortex is located close to the lower blade surface and has been shown to dynamically alter the blade pitching moment and corresponding pitch link loads as the blade passes through the reverse flow region [2,8]. The second vortex located above the rotor plane has not been studied intensively before. Based on its counterclockwise rotation and location above the rotor plane, it is neither a reverse flow dynamic stall vortex nor a tip vortex. Lind et al [27] found this vortex during a PIV investigation of an articulated slowed-rotor and called it a “reverse flow entrance vortex”. They postulated that its creation was linked to the entrance of the rotor blade into the reverse flow region, where it experienced flow conditions similar to the acceleration of a positively inclined airfoil from rest. Other than their previous work, there is perhaps no information about this type of vortex in literature and it is therefore investigated more closely here.

A series of phase-averaged flow fields recorded at the same operating conditions of $\mu = 0.5$, $\theta_0 = 10.6$ deg, and $\alpha_S = 4$ deg, but without fixed-wing, is shown in Fig. 12. The nine subfigures feature contour plots of the normalized vorticity component $\omega_z c_W / V_\infty$ and superimposed down-sampled in-plane velocity fields ($u - V_\infty$, v) over a quarter rotor rotation between $\Psi = 220$ deg and 300 deg blade azimuth. Laser shadows, rotor blades, and regions of bright reflections are masked with black color and the location of the rotor blade is highlighted in gray. A tip vortex (negative vorticity, blue color) is visible in multiple subfigures as it convects through the FOV above the rotor plane. The previously

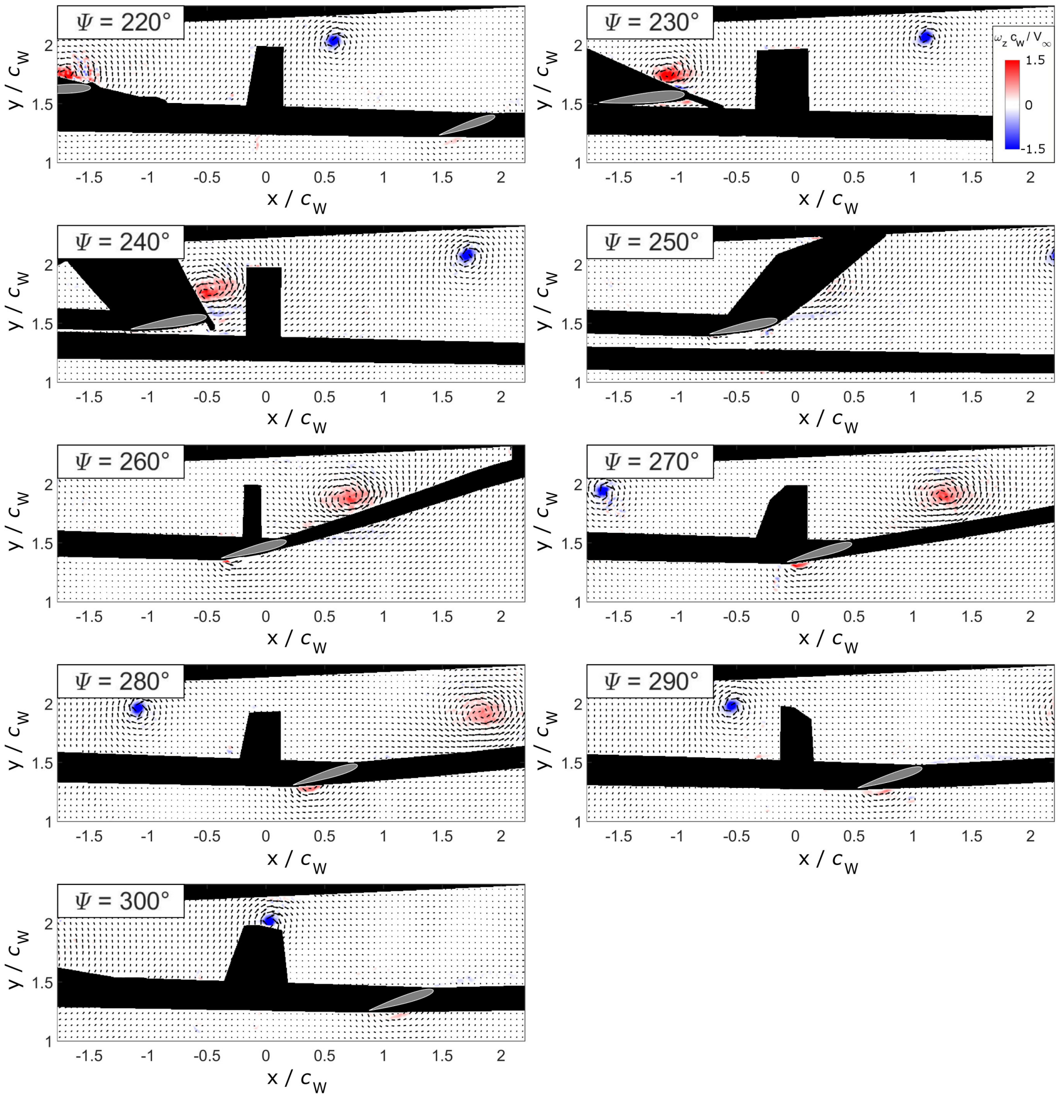

Fig. 12. Vorticity distribution and in-plane velocity field ($u - V_\infty$, v) over a quarter rotor revolution ($\mu = 0.5$, $\theta_0 = 10.6$ deg collective, $\alpha_S = 4$ deg shaft tilt, no fixed-wing)

described reverse flow dynamic stall vortex is also visible on the lower side of the rotor blade between $\Psi = 260$ deg and 290 deg. In addition, the previously called reverse flow entrance vortex appears in the majority of subfigures as a distinct region of positive vorticity with counterclockwise rotation (red color). Compared to the previous study by Lind et al [27], a larger FOV and corresponding azimuthal range was observed here, reaching up to an upstream location of 0.36R in front of the rotor hub or $x = -1.8c_W$ in the coordinate system of Fig. 12. The reverse flow region extends to a position of about $x = -1.4c_W$, which is located within the FOV. For the earliest recorded blade azimuthal positions at $\Psi = 220$ deg, the vortex is already fully formed and located at 0.3c_R on the rotor blade or $x = -1.72c_W$, well outside the reverse flow region. The creation of this vortex therefore occurs well ahead of the $\Psi = 220$ deg blade position and is not linked to entering the reverse flow region.

A more likely explanation is that this vortex forms due to classical dynamic stall on the retreating blade side. As no flow field information is available for earlier azimuthal positions, the blade sectional aerodynamics are examined at $\Psi = 220$ deg for the present test case to assess the conditions under which this vortex forms. The observed vortex is located at a lateral position of 0.3R, but at a radial blade position of 0.47R, with a blade sectional rotational speed of 0.47 $V_{tip} = 29.6$ m/s. The freestream velocity component along the blade chord is 19.94 m/s and effective chordwise velocity at this blade section thus becomes 9.02 m/s. Based on the recorded collective and cyclic pitch and neglecting blade deformations, the local blade pitch is $\theta = 10.7$ deg, but the effective angle of attack might be considerably increased by upwards-directed inflow through the rotor plane due to aft shaft tilt and fuselage-induced flow (e.g. vertical shaft tilt-induced flow of $\sin(\alpha_S)V_\infty = 2.5$ m/s would increase the effective angle of attack by about

Presented at 45th European Rotorcraft Forum, Warsaw, Poland, 17-20 September, 2019

13.5 deg at the present blade location). While these flow conditions might in general explain the occurrence of dynamic stall, the existence of a fully developed vortex at $\Psi = 220$ deg suggests onset of dynamic stall at even earlier azimuthal positions.

In a numerical study of an isolated 4-bladed articulated rotor at advance ratios of $\mu = 0.3 - 0.42$ and $C_L / \sigma \approx 0.1$, Richez [28] found a dynamic stall vortex in the inboard region of the retreating rotor blade that separated from the blade and convected downstream with the freestream velocity. In Richez' study, the occurrence of dynamic stall was linked to orthogonal blade-vortex interaction (BVI) between a tip vortex and rotor blade around $\Psi = 180$ deg rotor azimuth. The tip vortex increased the effective angle of attack outboard of the BVI location, causing the blade to undergo trailing edge dynamic stall. The stall spread radially and along the blade chord, reaching the leading edge between $\Psi = 210$ deg and 240 deg. Depending on the flow conditions, the dynamic stall vortex separated from the blade between $\Psi = 225$ deg and 270 deg rotor azimuth and overtook the blade within the reverse flow regime. This dynamic stall vortex was found to have a considerable radial extent on the blade and, for the $\mu = 0.42$ flow condition, interacted with the tip vortex after its separation from the rotor blade.

Although not all flow conditions and test stand properties are the same between the previous and current study, the general process of dynamic stall vortex formation could also apply here, explaining the early formation of this vortex, its considerable radial extent, as well as separation and interaction with the tip vortex downstream of the rotor blade. Further numerical and experimental studies are underway to confirm the origin of the present dynamic stall vortex and determine its impact on vibratory blade loads downstream of the reverse flow region. However, the formation of the dynamic stall vortex upstream of the reverse flow region indicates that it may not be the result of the rotor blade entering the reverse flow region.

The effects of advance ratio and shaft tilt on the flow field and vortex trajectories are examined in Figs. 13 and 14. The depicted results in Fig. 13 are similar to those shown in Fig. 12, but plotted in a moving coordinate system centered on the blade quarter chord position in the measurement plane. Each column of subfigures corresponds to a certain advance ratio and shaft tilt setting and shows a series of consecutive flow fields at blade azimuthal positions of $\Psi = 260$ deg to 290 deg. Figure 14 contains vortex trajectories corresponding to the test conditions presented in Fig. 13. The four subfigures contain data corresponding to tip vortices (black markers), as well as reverse flow or dynamic stall vortices (RF/DS) with fixed-wing (red markers) and without wing (blue markers) for 700 RPM (round markers) and 1200 RPM (square markers).

In the first column of Fig. 13 and corresponding top left graph of Fig. 14, the 0.3R radial station at $\mu = 0.3$ only experiences the onset of reverse flow and the convective velocity relative to the blade is close to zero. The locations of the tip, the dynamic stall, and the reverse flow dynamic stall vortices therefore do not change significantly with blade azimuth and only exhibit small-scale scattering. The main convective directions of vortices are also marked by arrows in Fig. 14. For the $\mu = 0.4$ case, a strong interaction between the tip and the dynamic stall vortices occurs above the rotor plane. The two vortices are less than one rotor chord length apart and form a strong downwash region in between. The location downstream of the blade and higher convective velocity than blade speed leads to insignificant effects on the 0.3R blade radial station. However, as shown in the top right graph of Fig. 14, the vortex pair and connected downwash region convect close to the rotor plane, possibly leading to BVI with outer blade sections downstream of the current measurement domain. For the $\mu = 0.5$ case, both tip vortex and dynamic stall vortex quickly move away from the current rotor blade, preventing significant interactions with it. The reverse flow dynamic stall vortex is the only vortex that remains close to the blade and therefore has a dominant and azimuth-dependent influence on the local blade loads. The final column and chart in Figs. 13 and 14 depicts a case with $\mu = 0.3$ and aft shaft tilt. Compared to the case at comparable advance ratio and zero shaft tilt, the tip vortex is located further from the rotor blade, the dynamic stall vortex has increased strength, and the reverse flow dynamic stall vortex is not present in most of the recorded images.

The strength of the tip and the dynamic stall vortices visible in Figs. 13 and 14 was quantified based on the peak swirl velocity around the detected vortex centers according to the process described in section 2.3. Figure 15 features graphs of peak swirl velocity $V_{\mathrm{Swirl,max}} / V_\infty$ over advance ratio for different rotor azimuths between $\Psi = 260$ deg and 290 deg. Each graph contains data points corresponding to the dynamic stall vortex (DSV, red markers) and tip vortex (TV, blue markers) for both $\alpha_S = 0$ deg (filled circles) and $\alpha_S = 4$ deg (unfilled circles) at $\theta_0 = 10.6$ deg and 700/1200 RPM. It is noted that some data points are missing in the figure due to obstruction by the rotor blades or the vortices being located outside the FOV. For the tip vortex, the peak swirl velocity drops from around $0.7 - 0.8\,V_\infty$ at $\mu = 0.3$ to $0.4 - 0.5\,V_\infty$ at $\mu = 0.5$, while no significant decrease in vortex strength is observed with wake age.

Presented at 45th European Rotorcraft Forum, Warsaw, Poland, 17-20 September, 2019

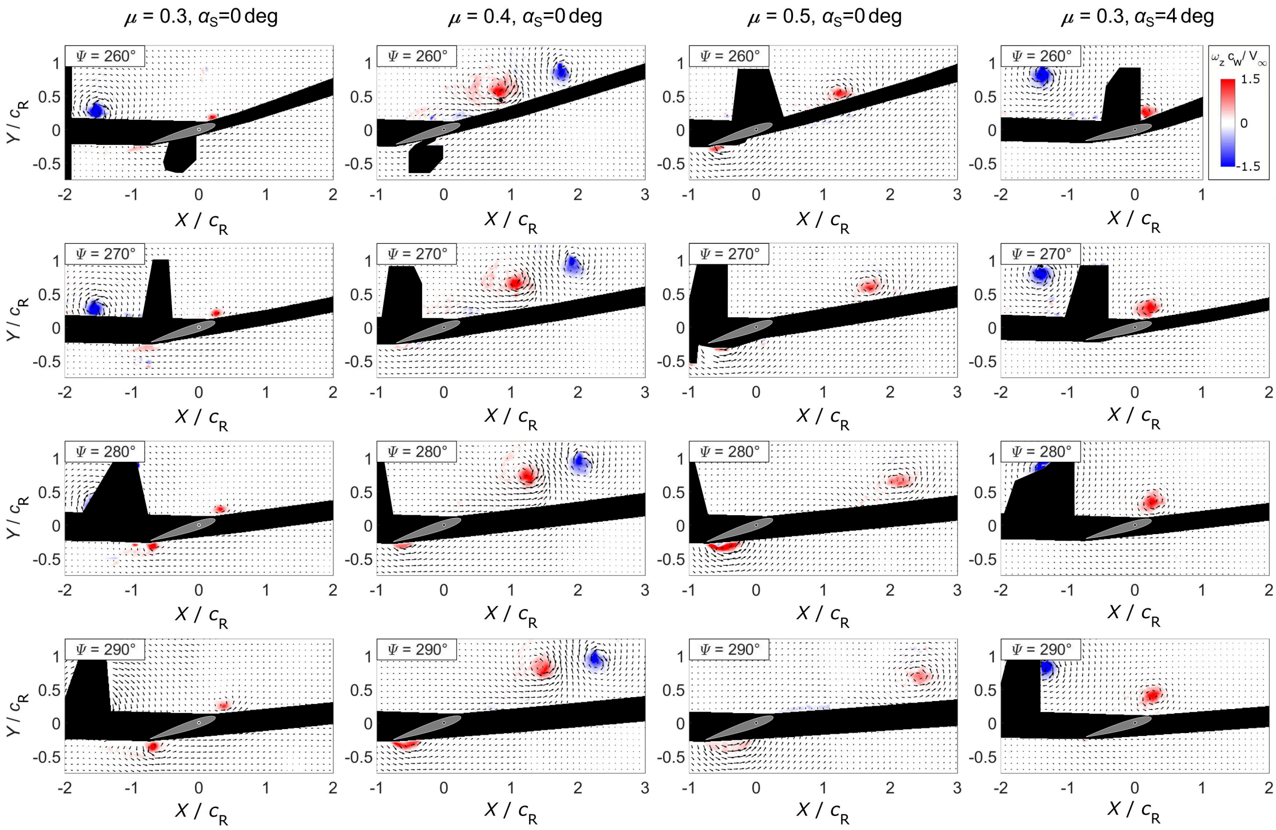

Fig. 13. Vorticity distribution around rotor blade from 260 deg to 290 deg rotor azimuth for $\theta_0 = 10.6$ deg collective and different advance ratios μ and shaft tilt angles α_S.

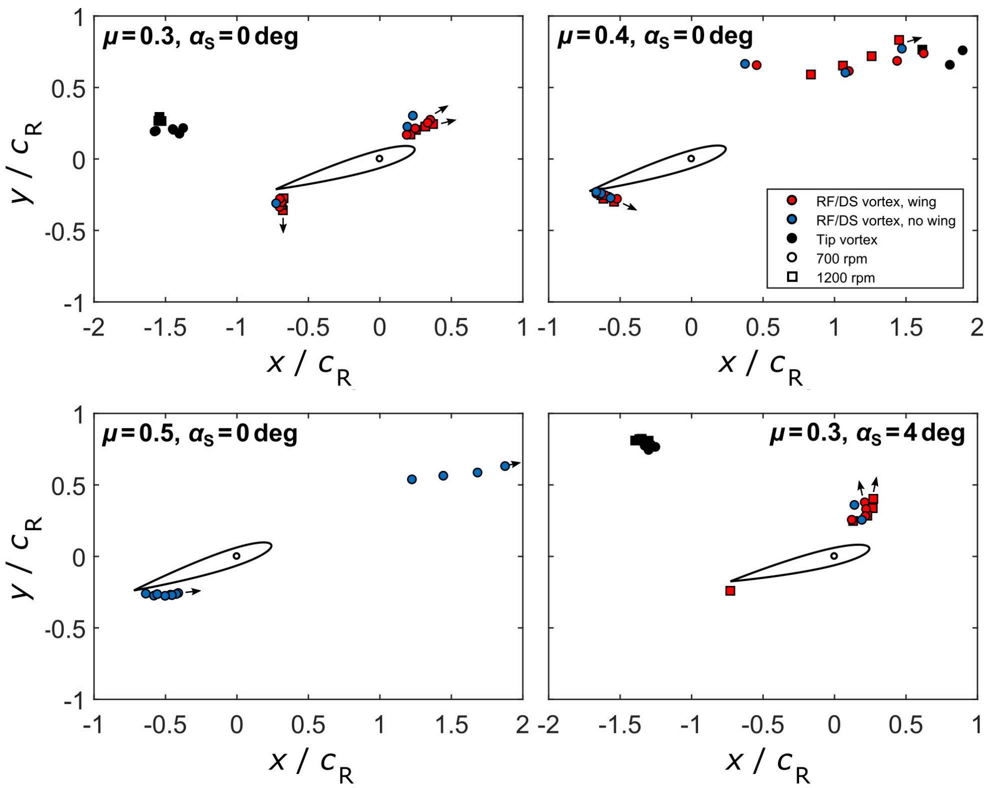

Fig. 14. Tracked vortex positions around rotor blade for $\theta_0 = 10.6$ deg collective and different advance ratios μ and shaft tilt angles α_S.

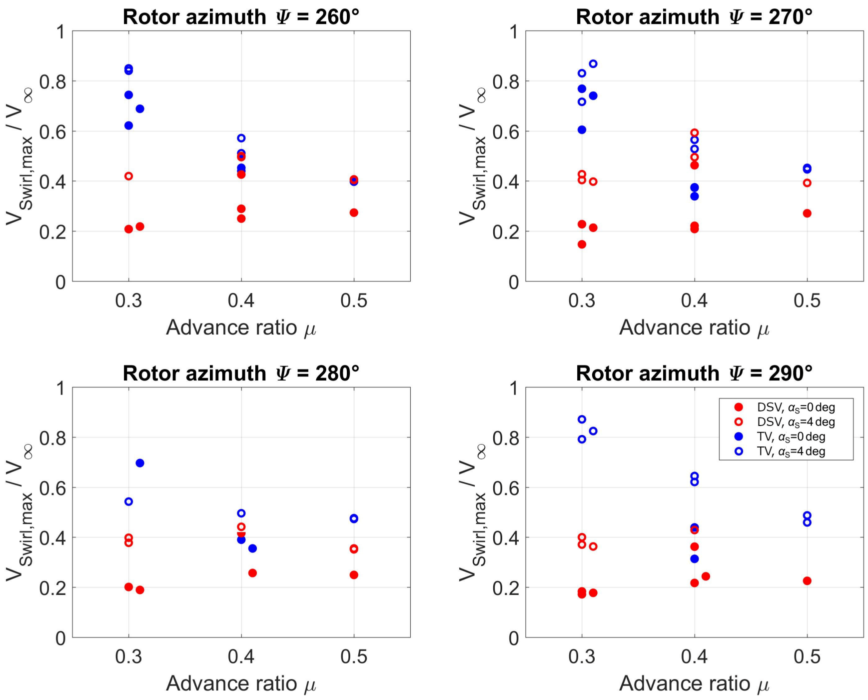

Fig. 15. Strength of tip vortex (TV) and dynamic stall vortex (DSV) over advance ratio for different rotor azimuth and shaft tilt at $\theta_0 = 10.6$ deg.

For most cases, aft shaft tilt increases the swirl velocity of the tip vortex by $0.1 - 0.2\,V_\infty$. The notable exception is for the $\Psi = 280$ deg case at $\mu = 0.3 - 0.4$, where the tip vortex is partially located in a masked-out region of the flow field and the evaluated peak swirl velocity is therefore too low.

For the dynamic stall vortex, the peak swirl velocity varies between 30% and 100% of the tip vortex values and the absolute vortex circulation Γ_V even surpasses the tip vortex strength. This is significant, as blade tip vortices are some of the dominant flow features in the rotor wake and their interaction with rotor blades (BVI) have wide-ranging effects such as increased blade vibratory loads and impulsive noise production [28,29]. The dynamic stall vortex investigated here therefore has the potential to also contribute to the blade vibratory loads, especially for blade azimuths where the blade is located downstream of the reverse flow region. The highest vortex strength is found for $\mu = 0.4$, where the dynamic stall vortex is located close to the tip vortex and the effects of both vortices are difficult to separate. Increased scatter in vortex strength at $\mu = 0.4$ and $\alpha_S = 0$ deg is caused by differences between cases with different rotor speed. Similar to the tip vortex, aft shaft tilt on average increases the peak swirl velocity by $0.1 - 0.2\,V_\infty$, leading to up to twice the vortex strength of the $\alpha_S = 0$ deg case.

The data presented in Figs. 13 – 15 shows that flow field properties around the rotor blade vary significantly with advance ratio. These non-linear effects pose a challenge for simple reduced order models that try to describe the relevant flow physics in the reverse flow region. It is found that the extent and strength of the dynamic stall and the reverse flow dynamic stall vortices vary with advance ratio and shaft tilt. At least for the current radial measurement position, the dynamic stall vortex above the rotor plane can reach equal or higher strength than the tip and the reverse flow dynamic stall vortices, although it only remains close to the airfoil at the critical radial location where the blade has the same velocity as the freestream. Further interactions of the dynamic stall vortex with outer parts of the rotor blade are expected downstream of the reverse flow region. Based on the strength of the dynamic stall vortex, these interactions could impact blade vibratory loads and should be investigated in future studies.

4. CONCLUSIONS

A lift-compound helicopter model with hingeless rotor and a single fixed-wing on the retreating blade side was tested in the Glenn L. Martin wind tunnel at the University of Maryland. The 0.84 m radius 4-bladed rotor was operated at 700 RPM and 1200 RPM at advance ratios of $\mu = 0.3 - 0.5$. The fixed-wing with a span of 0.7R was installed 0.24R below the rotor plane with a fixed pitch of 8 deg. Based on data collected from the rotor test stand, instrumented rotor blades, and flow field measurements on the retreating blade side

Presented at 45th European Rotorcraft Forum, Warsaw, Poland, 17-20 September, 2019

between the fixed-wing and rotor plane, the impact of operational and rotor parameters on performance and aerodynamics of the system was examined and mutual interaction effects between rotor and fixed-wing were analyzed. Some key conclusions are summarized here:

- The rotor downwash reduces fixed-wing lift by up to 23% at $\mu = 0.3$ and increases wing vibratory loads, while the fixed-wing is found to influence the effective angle of attack of the retreating rotor blade by up to 2 deg.

- The present fixed-wing position at –24%R below the rotor hub is found to be adequate for $\mu = 0.5$, with rotor downwash affecting wing lift by less than 4%.

- The combination of finite rolling moment trim (offset-trim) and aft shaft tilt increases rotor lift coefficient by up to 79% at 6 deg rotor collective and the corresponding peak lift-to-drag ratio of the compound rotorcraft is improved by up to 60% for zero shaft tilt and 45% at 4 deg aft shaft tilt at $\mu = 0.5$.

- For a fixed total vehicle lift of 133 N (30 lb), a lift share value of 23% reduces the required rotor collective by 20% for zero shaft tilt and 64% for 4 deg aft shaft tilt, while increasing overall lift-to-drag by up to 32% for both shaft tilt angles.

- Aft shaft tilt reduces rotor shaft torque by up to 55% at constant lift. This effect persists for offset-trim conditions. The fixed-wing drag partially counteracts main rotor torque, reducing the required yaw moment for trimmed forward flight.

- The comprehensive analysis, the in-house code UMARC, has been expanded to also cover main effects of the added fixed-wing. The updated wing characteristics are based on CFD results for an isolated fixed-wing and are able to capture general performance trends of the compound rotorcraft.

- The flow field analysis reveals a dynamic stall vortex that freely convects through the reverse flow region and rivals the strength of blade tip vortices. Contrary to previous beliefs, this vortex originates upstream of the reverse flow region and its detachment from the rotor blade is related to entering the reverse flow region.

- Advance ratio and shaft tilt angle are found to have significant and non-linear impact on the dynamic stall vortex and its interactions with blade tip vortices and the rotor blade. Further research is necessary to determine the exact origin of this dynamic stall vortex and to study its effects on blade vibratory loads downstream of the reverse flow region.

The present work highlights the effects of adding a hingeless rotor and single-fixed wing to a high-speed rotorcraft and demonstrates that significant improvements in overall vehicle performance are feasible.

ACKNOWLEDGEMENTS

This work was supported by the Army/Navy/NASA Vertical Lift Research Center of Excellence (VLRCOE) with Mahendra Bhagwat as technical monitor. Further support was provided by Deutsche Forschungsgemeinschaft (DFG) under grant no. BA6090/1-1. The authors would like to thank Vikram Hrishikeshavan, Shashank Maurya, and the staff of the Glenn L. Martin Wind Tunnel for their valuable assistance during the wind tunnel test.

COPYRIGHT STATEMENT

REFERENCES

[1] F. J. Perry, "Aerodynamics of the Helicopter Speed Record," in *American Helicopter Society 43rd Annual Forum*, Alexandria, VA, May 1987, pp. 1–13.

[2] A. Datta, H. Yeo, and T. R. Norman, "Experimental Investigation and Fundamental Understanding of a Full-Scale Slowed Rotor at High Advance Ratios," *J. Am. Helicopter Soc.*, vol. 58, no. 2, 2013, pp. 1–17.

[3] L. N. Trollinger, "Refined performance and loads of a mach-scale rotor at high advance ratios," Master thesis, University of Maryland, Department of Aerospace Engineering, 2017.

[4] S. Kottapalli, "Performance and Loads Correlation of a UH-60A Slowed Rotor at High Advance Ratios," in *AHS Future Vertical Lift*

Aircraft Design Conference, San Francisco, CA, January 2012, pp 1–33.

[5] M. Potsdam, A. Datta, and B. Jayaraman, “Computational investigation and fundamental understanding of a slowed UH-60A rotor at high advance ratios,” *J. Am. Helicopter Soc.*, vol. 61, no. 2, 2016, pp. 1–17.

[6] D. Walsh, S. Weiner, K. Arifian, *et al.*, “High Airspeed Testing of the Sikorsky X2 TechnologyTM Demonstrator,” in *American Helicopter Society 67th Annual Forum*, Virginia Beach, VA, May 2011, pp. 1–12.

[7] A. H. Lind, J. N. Lefebvre, and A. R. Jones, “Time-Averaged Aerodynamics of Sharp and Blunt Trailing-Edge Static Airfoils in Reverse Flow,” *AIAA J.*, vol. 52, no. 12, 2014, pp. 1–14.

[8] B. Berry and I. Chopra, “Slowed Rotor Wind Tunnel Testing of an Instrumented Rotor at High Advance Ratio,” in *Proc. 40th European Rotorcraft Forum*, Southampton, UK, September 2014, pp. 1–12.

[9] A. Sridharan, B. Govindarajan, V. T. Nagaraj, and I. Chopra, “Design considerations of a lift-offset single main rotor compound helicopter,” in *American Helicopter Society International - AHS Specialists’ Conference on Aeromechanics Design for Vertical Lift,* San Francisco, CA, January 2016, pp. 1–18.

[10] S. Jo and K. Choi, “Investigation of Compound Rotorcraft with Asymmetric Wing and Single Rotor,” in *7th Asian/Australian Rotorcraft Forum*, Jeju Island, Korea, October 2018, pp. 1–6.

[11] X. Wang, A. Bauknecht, S. Maurya, and I. Chopra, “Wind Tunnel Test on a Slowed Mach-Scaled Hingeless Rotor at High Advance Ratios,” in *Vertical Flight Society 75th Annual Forum & Technology Display*, Philadelphia, PA, May 2019, pp. 1–10.

[12] C. E. Freeman and R. E. Mineck, “Fuselage surface pressure measurements of a helicopter wind-tunnel model with a 3.15-meter diameter single rotor,” Hampton, VA, NASA TM80051, March 1979, pp. 1–170.

[13] J. Jeong and F. Hussain, “On the identification of a vortex,” *J. Visalization*, vol. 285, 1995, pp. 69–94.

[14] B. G. van der Wall and H. Richard, “Analysis methodology for 3C-PIV data of rotary wing vortices,” *Exp. Fluids*, vol. 40, 2006, pp. 798–812.

[15] G. H. Vatistas, V. Kozel, and W. C. Mih, “A simpler model for concentrated vortices,” *Exp. Fluids*, vol. 11, no. 1, 1991, pp. 73–76.

[16] W. Kaufmann, “Über die Ausbreitung kreiszylindrischer Wirbel in zähen (viskosen) Flüssigkeiten,” *Ingenieur-Archiv*, vol. 31, no. 1, 1962, pp. 1–9.

[17] M. Scully and J. P. Sullivan, *Helicopter rotor wake geometry and airloads and development of laser Doppler velocimeter for use in helicopter rotor wakes*. MIT Aerophysics Laboratory, Cambridge, MA, TR179, August 1972, pp. 1–67.

[18] A. Bagai and J. G. Leishman, “Rotor Free-Wake Modeling Using a Pseudo-Implicit Technique - Including Comparisons with Experimental Data,” *J. Am. Helicopter Soc.*, vol. 40, no. 3, 1995, pp. 29–41.

[19] X. Wang and J. Baeder, “Correlation of Predictions with Measured Pressure Data from a Slowed Mach-Scaled Rotor at High Advance Ratios,” in *Aeromechanics Design for Transformative Vertical Flight Technical Meeting Proceedings*, San Francisco, CA, January 2018, pp. 1–8.

[20] G. Bowen-Davies and I. Chopra, “Investigation of the UH-60A Slowed Rotor Wind Tunnel Tests using UMARC,” in *American Helicopter Society 69th Annual Forum*, Phoenix, AZ, May 2013, pp. 1–13.

[21] J. Weissinger, “The lift distribution of swept-back wings,” NACA, Washington D.C., TM 1120, March 1947, pp. 1–51.

[22] T. S. Beddoes and J. G. Leishman, “A Semi-Empirical Model for Dynamic Stall,” *J. Am. Helicopter Soc.*, vol. 34, no. 3, 1989, pp. 3–17.

[23] X. Wang, Y. S. Jung, J. Baeder, and I. Chopra, “CFD Pressure/Airload Correlation with Experimental Data on a Slowed Mach-Scaled Rotor at High Advance Ratios,” in *Vertical Flight Society 74th Annual Forum & Technology Display*, Phoenix, AZ, May 2018, pp. 1–9.

[24] B. Berry and I. Chopra, “Wind Tunnel Testing of an Instrumented Rotor at High Advance Ratio,” in *Proc. 56th AIAA/ASCE/AHS/ASC Structures, Structural Dynamics, and Materials Conference*, Kissimmee, FL, January 2015, pp. 1–14.

[25] Y. Yu, C. Tung, B. Van Der Wall, and H. Pausder, “The HART-II test: Rotor wakes and aeroacoustics with higher-harmonic pitch control (HHC) inputs - The joint german/french/dutch/us project,” in *Proc. American Helicopter Society 58th Annual Forum*, Montreal, Canada, June 2002, pp. 1–13.

[26] L. Smith, Y. S. Jung, J. D. Baeder, and A. R. Jones, “Vorticity Transport in the Reverse Flow Region of a Rotor at High Advance Ratio,” in *AIAA Scitech 2019 Forum*, San Diego, CA, January 2019, pp. 1–14.

[27] A. H. Lind, L. N. Trollinger, F. H. Manar, I. Chopra, and A. R. Jones, “Flowfield measurements of reverse flow on a high advance ratio rotor,” *Exp. Fluids*, vol. 59, no. 12, 2018, pp. 1–15.

[28] F. Richez, “Numerical analysis of dynamic stall for different helicopter rotor flight conditions,” in *AHS International 73rd Annual Forum & Technology Display*, Fort Worth, TX, May 2017, pp. 1–16.

[29] A. R. George, “Helicopter Noise: State-of-the-Art,” *J. Aircr.*, vol. 15, no. 11, 1978, pp. 707–715.

Presented at 45th European Rotorcraft Forum, Warsaw, Poland, 17-20 September, 2019